

Fast Raman transitions for Ramsey interferometry

Jan Uckert

Masterarbeit in Physik
angefertigt im Institut für Angewandte Physik

vorgelegt der
Mathematisch-Naturwissenschaftlichen Fakultät
der
Rheinischen Friedrich-Wilhelms-Universität
Bonn

November 2019

I hereby declare that this thesis was formulated by myself and that no sources or tools other than those cited were used.

Bonn,
Date

.....
Signature

1. Gutachter: Prof. Dr. Dieter Meschede
2. Gutachter: Prof. Dr. Simon Stellmer

Contents

1	Introduction	1
2	Theory and experimental apparatus	3
2.1	Optical lattices	3
2.1.1	Optical dipole potential	3
2.1.2	Scattering with lattice photons	5
2.1.3	From the background into the lattice	6
2.1.4	Caesium in the optical lattice	6
2.1.5	State detection	7
2.1.6	State dependent lattice	8
2.2	Qubit states and Bloch representation	9
2.3	Ramsey interferometry	10
2.3.1	Measurement of coherence relaxation time	11
2.4	Quantum speed limit	12
3	Raman laser setup	15
3.1	Raman transitions	15
3.2	Raman transitions in Caesium	19
3.3	Optical setup	20
3.3.1	AOM in double pass configuration	22
3.3.2	Control circuitry of the AOM	22
3.3.3	Optical phase lock loop	23
3.3.4	Cleaning the lattice control loop	26
3.4	Characterization	28
3.4.1	Calculation of induced light shift and Rabi frequency	28
3.4.2	Light shift from Raman beams	29
3.4.3	Raman laser phase stability	32
3.4.4	Long-term stability of the lasers	33
3.4.5	Power calibration of Raman beams	33
3.4.6	Time calibration for Raman pulses	34
4	Experimental Procedure	37
4.1	Raman spectroscopy	37
4.2	Rabi oscillation measurement	41
4.3	Raman thermometry	43

4.4	Ramsey interferometry	46
4.4.1	Measurement scheme for quantum speed limit	46
4.4.2	Phase modulation	47
4.4.3	Fast Ramsey fringes	49
4.4.4	Quantum speed limit measurements	50
5	Summary and outlook	55
	Bibliography	59

Introduction

The concepts of quantum mechanics were presented and developed in the first half of the 20th century. Through the efforts of Heisenberg, Schrödinger, Dirac, all of whom received Nobel prizes for their work, and several others, many unexplained phenomena and questions were resolved. Our understanding of the natural world grew immensely, but of course, with the new physics, new questions arose as well. New frontiers in research were opened up, and it was famously Richard Feynman who suggested solving complex physical problems in a new way:

"The rule of simulation that I would like to have is that the number of computer elements required to simulate a large physical system is only to be proportional to the space-time volume of the physical system. I don't want to have an explosion." - Richard Feynman, 1982

In essence, he proposed to use quantum computers to simulate the dynamics of quantum systems instead of using classical computers. The advantage is that the time it would take to factor large numbers rises exponentially with their size in the case of a classical computer, while it rises only linearly for quantum computers. There are several avenues of research to realize such a system, from micro potentials, [1] and [2], to trapped ions [3] and also trapped neutral atoms in optical lattices. In recent years, optical lattice potentials have successfully been used in several fields, such as metrology, to realize the most accurate clocks to date [4], or quantum simulation, by simulating the Hamiltonians of other systems like solid state systems [5] or topological quantum insulators [6].

The quantum technologies group at the IAP in Bonn is experienced in the investigation of few-body quantum systems. A thorough understanding and precise control of such systems is a vital part of determining the viability of ultracold atomic gases in optical lattices as a platform to realize a universal quantum computer. The one-dimensional optical lattice experiment, where I did my work, has in recent years produced advances and improvements in the area of optical lattices, state-dependent transport and optimal quantum control. Since its experimental setup is fully functional and operated by experienced personnel, it presented a promising environment to do research and the work for my Master's thesis. In cooperation with Technion from Haifa, we set out to make modifications on the existing setup. The plan was to investigate the possibilities of using Raman transitions to access our qubit on the D2 line of Cesium, to induce Rabi oscillations at Rabi frequencies far beyond the former capabilities of the setup and to perform Ramsey interferometry with the goal of probing the Mandelstam-Tamm quantum speed limit.

This limit, derived by Mandelstam and Tamm in 1945 [7], describes a fundamental boundary to the

speed at which a wave function may evolve from its initial to an orthogonal state. Fascinating as such a principle would be on its own, it gains even more significance through its implications for the development of new technologies. Machines of a kind as Feynman suggested would have an upper limit on their computational speed. Because of this, research in this area is an exciting and important milestone on the way to quantum computers.

Outline The content of this thesis will be divided into 3 parts. In the first chapter, I will go over the theory behind the optical lattice setup, how the experiment is designed and the necessary steps towards an experiment-ready atom sample. I will also cover the derivation of the quantum speed limit. The second chapter will treat the design, operation and calibration of the Raman laser setup, which was modified to perform fast pulses, phase modulation of these pulses and ultimately Ramsey interferometry.

The third chapter treats the experiments performed with the aforementioned laser setup, the results and analysis.

At the end, I will give a short summary and an outlook on the next possible steps to take with the working setup and which further experiments might be performed.

Theory and experimental apparatus

This first chapter will treat the theoretical foundations of my work and the principles and methods involved in the operation of the experimental setup.

2.1 Optical lattices

2.1.1 Optical dipole potential

Optical lattices are created through the interference of counter-propagating laser beams. In this configuration, their interference pattern forms a periodic potential which can be used in atom trapping, cooling and transporting. The dipole potentials arise as a result of the interaction of the atoms with the far detuned electromagnetic fields. This process can be understood semi-classically, following [8]. When the atoms are exposed to the laser, the electric field $E(x, t) = \hat{e}E_0(x)\cos(\omega t)$ induces the atomic dipole moment $\mu(x, t) = \hat{e}p(x)$, oscillating with frequency ω and amplitude $p(x) = \alpha(\omega)E(x)$. Here α is the atomic polarizability. The resulting potential is then:

$$U_{\text{dip}}(x) = -\frac{1}{2}\langle \mu(x, t) \cdot E(x, t) \rangle_t = -\frac{1}{2\epsilon_0 c} \text{Re}(\alpha(\omega))I(x) \quad (2.1)$$

Where $\langle \rangle_t$ denotes the time average and $I(x) = 2\epsilon_0 c |E(x)|^2$ is the intensity of the electric field.

It follows that the dipole force is:

$$F_{\text{dip}}(x) = -\nabla U_{\text{dip}}(r) = \frac{1}{2\epsilon_0 c} \text{Re}(\alpha(\omega))\nabla I(x) \quad (2.2)$$

It is a conservative force dependant on the atomic polarizability and the intensity gradient of the light field. Treating the atom as a two-level quantum system interacting with a classical light field, we can express the polarizability in terms of the scattering rate Γ :

$$\alpha = 6\pi\epsilon_0 c^3 \frac{\Gamma/\omega_0^2}{\omega_0^2 - \omega^2 - i(\omega^3/\omega_0^2)\Gamma} \quad (2.3)$$

Where the scattering rate is being calculated through the dipole matrix element between ground state and excited state:

$$\Gamma = \frac{\omega_0^3}{3\pi\epsilon_0\hbar c^3} |\langle e|\mu|g\rangle|^2 \quad (2.4)$$

These expressions allow us now to put the dipole potential in terms of the scattering rate, the intensity of the electric field and the detuning between the laser and the resonance frequency of the transition Δ . Also using the rotating wave approximation to neglect the counter rotating term yields:

$$U_{\text{dip}}(x) = \frac{3\pi c^2}{2\omega_0^3} \frac{\Gamma}{\Delta} I(x) \quad (2.5)$$

We can now draw some conclusions about the nature of our system. It is clear that a higher intensity will cause a deeper trap and allow us to trap faster atoms, but the frequency of the trapping light is also important. Using a laser that is red detuned from the transition frequency will cause the resulting potential to be attractive, while a blue detuned laser will result in a repulsive potential.

More insight can be gained from a quantum mechanical treatment. The dipole potential as a result of the atom light interaction can be described as a shift in the energy levels of the atoms, the AC-stark effect. This energy shift can be calculated using second order perturbation theory and the Hamiltonian of the atom-light interaction \mathcal{H}_{int} . The light induced energy shift is then:

$$\Delta E_{\text{ind}} = \sum_{j \neq i} \frac{1}{\hbar} \frac{|\langle j|\mathcal{H}_{\text{int}}|i\rangle|^2}{\omega - \omega_{i \rightarrow j}} \quad (2.6)$$

Here $\hbar\omega$ is the energy of a single photon of the incident laser and $\hbar\omega_{i \rightarrow j}$ the energy difference between the i th and the j th energy levels of the atom. Reducing this general problem to a two level-system of only a ground state and an excited state and using again the rotating wave approximation, we get:

$$\Delta E_{\text{ind}} = \pm \frac{1}{\hbar} \frac{|\langle e|\vec{d}|g\rangle|^2}{\Delta} |E_0|^2 = \pm \frac{6\pi c^2}{\omega_0^3} \frac{\Gamma}{\Delta} I \quad (2.7)$$

We can see now that if we choose a laser frequency red detuned from the transition frequency between the ground and excited states $\hbar\omega_{\text{red}}$, the resulting potential is an attractive one for the ground state, for the excited state however it is repulsive, see figure 2.1, marked in red. The opposite result is found for a blue detuned frequency $\hbar\omega_{\text{blue}}$, as seen in figure 2.1 marked in blue.

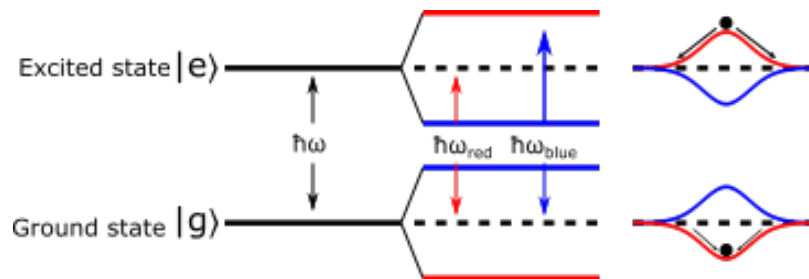


Figure 2.1: Light shifts of two-level atom interacting with an off resonant electromagnetic field

In our setup, the potential is produced by two counter-propagating gaussian laser beams at 866nm. They are focused in the vacuum glass chamber to a beam waist of about $17\mu\text{m}$. The lattice constant is $\lambda/2$ and the Rayleigh length 1.04mm . Considering then the fact that all transport operations and experiments in this thesis take place over a region of at most 200 lattice sites, we can ignore in good approximation any contributions from the curved wavefront and the Guoy phase of the beams. The lattice potential is a result of the interference of the overlapping beams and forms a periodic cosinusoidal potential in the longitudinal (x) direction, while in the transverse direction (ρ), it is a direct result of the laser's intensity profile:

$$U(x, \rho) = U_0 \frac{\omega_{DT}^2}{\omega^2(x)} e^{\frac{-2\rho^2}{\omega_0^2(x)}} \cos^2\left(\frac{2\pi}{\lambda_{DT}}x\right) \quad (2.8)$$

2.1.2 Scattering with lattice photons

Following equation 2.7, we see a high laser intensity produces deeper trapping potentials and seems like an obvious way to improve trapping strength. Calculating, however, the scattering rate of atoms with the lattice photons themselves, we see:

$$\Gamma_{\text{scat}} = \frac{6\pi c^2}{\omega_0^3} \left(\frac{\Gamma}{\Delta}\right)^2 I \quad (2.9)$$

Similar to the potential depth, the scattering rate is directly proportional to the intensity. In contrast, there is a quadratic dependence over the fraction $\frac{\Gamma}{\Delta}$, so a high detuning will alleviate the effect of the high intensity. Scattering of the lattice photons would lead to heating of the atoms by two times E_{rec} , the recoil energy, given by:

$$E_{\text{rec}} = \frac{h^2}{2M\lambda_{dt}^2} \quad (2.10)$$

The inelastic scattering of a photon will lead to a change in the atom's internal state and to a population decay of the prepared states. The population relaxation time T_1 is a measure of that process and tells us the characteristic time for the decay of a prepared population in a given spin state:

$$P_{\uparrow}(t) = P_{\text{eq}} - (P_{\text{eq}} - P_{\downarrow})e^{-\frac{t}{T_1}} \quad (2.11)$$

Where P_{eq} is the equilibrium ratio between the states P_{\uparrow} and P_{\downarrow} .

In the elastic case, we speak of Rayleigh scattering, the internal state is unaffected. But since the atom's quantum state is effectively measured, it leads to a decoherence in both the spin and position states. The uncertain position of the atom is projected into a single lattice site, destroying spatial coherence and leading to dephasing. Following [9], a model for the decoherence is directly proportional to the intensity:

$$\delta_{\text{dec}} \propto I \left(\frac{1}{\Delta_{D2}^2} - \frac{1}{\Delta_{D1}^2} \right) \quad (2.12)$$

Where Δ_{D2} and Δ_{D1} are the detuning of the lattice beams to the $D2$ and $D1$ lines of Caesium.

The potential depths of our lattice are $U_0/k_B = 370\mu\text{K}$ at 30mW power per beam, which we call the deep lattice. It is used for the trapping and imaging of the atoms. The second setting is $U_0/k_B = 74\mu\text{K}$ at 6mW power per beam, the shallow lattice, which is where we can control the quantum state of the atoms more precisely due to the reduced scattering with the trapping beams themselves, since the intensity is lower.

2.1.3 From the background into the lattice

Since the mean velocity of Caesium at room temperature is about 200m/s , loading the lattice directly from the background gas would be very inefficient. It needs to be cooled first. For this, we employ three pairs of circularly polarized laser beams tuned to the D2 line of Caesium, which cool the atoms through repeated isotropic emission of photons and a pair of magnetic coils in anti-Helmholtz configuration that produce a quadrupole field to lift the degeneracy of the Zeeman sublevels, the red contour in fig 2.2. Atoms at different points in the magnetic field experience a different radiation pressure from light of different circular polarizations, with a net force pushing the atoms to the center. A more detailed description of the physical mechanisms of a MOT can be found in [10] or [11]. The limit for this cooling method is the well known Doppler limit, which in our case lies at $125\mu\text{K}$.

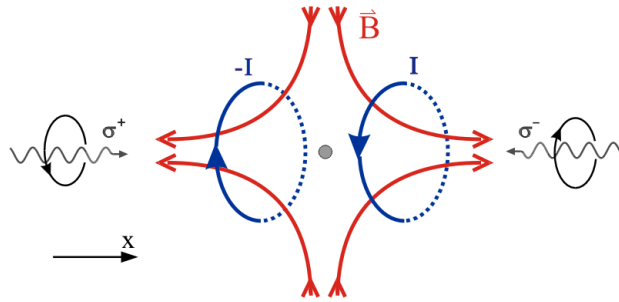


Figure 2.2: Field and laser beam configuration for a MOT [12]

At this point, the gradient fields are turned off and the atoms are transferred into the lattice. With a good overlap between the thermal distribution of the atoms after the cooling process and the possible amount of trapped states, we get an average loading of 20 – 60 atoms in the camera's field of view. From that point, we use the Molasses beams on a different setting and employ sub-Doppler cooling as explained in [13]. The three pairs of molasses beams create polarization gradients and cool the atoms to below $10\mu\text{K}$.

A further cooling step, once the atoms are in the lattice, is the microwave sideband cooling, which transfers the atoms into their vibrational ground state. For the purpose of this thesis, this was not required, so for a description of the process in this setup, see [14]

2.1.4 Caesium in the optical lattice

The experimental medium in our optical lattice is Caesium. Due to its narrow linewidth, the $|F = 3\rangle$ to $|F = 4\rangle$ transition is an ideal candidate for experimentation [15]. The hyperfine splitting is

$\Delta\nu_{HF} = 9.19263177\text{GHz}$, which we can easily address using our two lasers by simply detuning them from each other by that amount.

To have a qubit that can be accessed with the state dependent methods discussed in chapter 2.1.6, we need two states with a non vanishing angular momentum [14], so we chose the two hyperfine sublevels $|F = 4, m_F = 4\rangle$ and $|F = 3, m_F = 3\rangle$, which will be called the $|\uparrow\rangle$ and $|\downarrow\rangle$ states. We decided on these two outermost sublevels because during the state preparation with F - and m_F -pumping laser beams, these two states can be most easily accessed, since the $|\uparrow\rangle$ is the dark state of the pumping process.

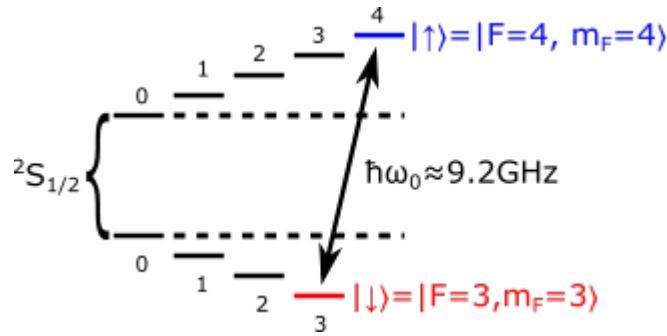


Figure 2.3: Qubit level scheme for Caesium

The state preparation methods have been extensively covered in [14], but I will cover the basics here nonetheless. During fluorescence image acquisition and the adiabatic lowering of the lattice, all external magnetic fields are suppressed using an array of compensation coils. That means the trapped atoms freely undergo σ_+ , σ_- and π transitions, off-resonantly scatter with lattice photons and equally populate the $|F = 3\rangle$ and $|F = 4\rangle$ hyperfine sublevels. Following [16] and [17], we use F - and m_F -pumping, preparing the atoms in the desired states with a fidelity of $> 99\%$. Such high fidelities can only be achieved if the quantization axis is aligned to the optical pumping beams, which is done by using the compensation coils to generate a guiding magnetic field with a field strength of $|B_0| = (2.95 \pm 0.02)G$.

For the F -pumping we need light, locked to the $|F = 3\rangle$ to $|F' = 4\rangle$ transition. So we extract a part of the MOT-light and use up to around 10nW for the F -pumping. The m_F -pumping is realized by a σ_+ polarized beam, resonant to the $|F = 4\rangle$ to $|F' = 4\rangle$ transition. 1nW of that are overlapped with the light from the F -pumping and the quantization axis, and after pumping lengths of 20ms , $> 99\%$ of the atoms are in the $|\uparrow\rangle$ -state, which is the dark state of the pumping scheme.

2.1.5 State detection

To verify the effect of the optical pumping and for any other application in this thesis in which the state population is measured, we employ the Push-Out technique [18]. Here, a short laser pulse, $40\mu\text{W}$ for $400\mu\text{s}$, resonant with the $|F = 4\rangle$ to $|F' = 5\rangle$ transition, is used. It is being applied from a radial direction with a very high intensity ($I/I_0 = 100$). Atoms in the $|\uparrow\rangle$ are pushed out of the optical lattice by the radiation pressure, while the atoms in the $|\downarrow\rangle$ state remain with a fidelity of $> 99\%$.

The remaining atoms in $|\downarrow\rangle$ are then observed through fluorescence imaging, determining the

percentage of the initial atoms that were occupying the $|\uparrow\rangle$ state.

2.1.6 State dependent lattice

State dependent lattices have been introduced by Jaksch et al. [19] and Deutsch et al. [20]. We improve on earlier methods of state dependent transport through an approach based on a high precision, large bandwidth synthesizer of polarization states, for details see [21]. A linearly polarized beam is overlapped with 2 circularly polarized beams of opposite circular polarizations by having them enter the vacuum chamber from opposite ends. We control the polarization state of the superposition of the two beams by controlling the phase of the two individual beams. Since a linear polarization can be described as the superposition of two circular polarizations of opposite circularities, the result is two overlapping optical lattices, one with σ_+ , one with σ_- polarization.

Ideally, the atoms in the two hyperfine levels $|\uparrow\rangle := |F = 4, m_f = 4\rangle$ and $|\downarrow\rangle := |F = 3, m_f = 3\rangle$ (see fig. 2.4) are only affected by σ_+ or σ_- polarized light respectively. That way, preparing two overlapping lattices with these two different polarizations, we are able to move the potentials affecting the atoms in each of the two spin states independently.

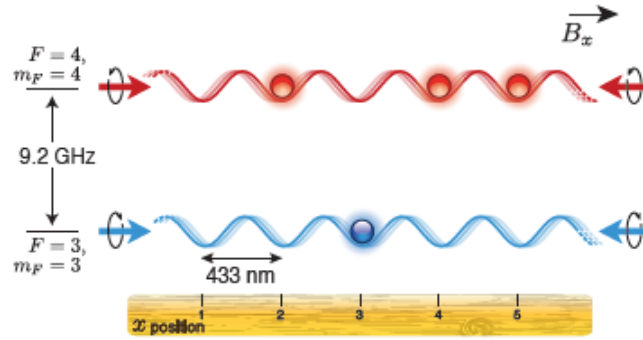


Figure 2.4: State dependent lattice [14]

While a separation like that is possible for fine structure states, a direct mapping on the hyperfine states onto the fine structure reveals that the states are still coupled. Calculations yield a magic wavelength of $\lambda = 865.9\text{nm}$, at which the potentials for the two different states take the following form:

$$U_{\uparrow} = U_{\sigma_+} \quad (2.13)$$

$$U_{\downarrow} = \sqrt{\frac{7}{8}}U_{\sigma_-} + \sqrt{\frac{1}{8}}U_{\sigma_+} \quad (2.14)$$

The atoms in the upper qubit state are completely decoupled from the σ_- light, but in the lower state, there is still a contribution from the σ_+ light.

Our experiments are performed in a deep enough lattice that tunneling between lattice sites is negligible. So the position of atoms in the $|\uparrow\rangle$ and $|\downarrow\rangle$ states is dependent on the position of the σ_+ and σ_- lattices.

2.2 Qubit states and Bloch representation

Once initialized in the $|\uparrow\rangle$ state, there is always the present risk of unwanted transitions to the other sublevels. To regain high occupancy levels in the desired states, and since we designed the state dependent lattice only to affect the $|\downarrow\rangle$ and $|\uparrow\rangle$ states, we want to spectrally separate the m_F sublevels. The magnetic guiding field of the quantization axis with a field strength of $|B_0| = 3\text{G}$ lifts the degeneracy of the sublevels and separates neighbouring sublevels by 1.05MHz [22].

This separation is also advantageous for the mathematical treatment, since we can now reduce the Hilbert space to a two-level system and describe the superposition state of $|\uparrow\rangle$ and $|\downarrow\rangle$ as:

$$|\Psi\rangle = c_1|\uparrow\rangle + c_2|\downarrow\rangle \quad (2.15)$$

This pseudo spin-1/2 system can be described using the Bloch equations [23], which can be derived from the Heisenberg uncertainty relation using the rotating wave approximation. Since in our system, relaxation effects of both the population and the coherence influence the dynamics, we include them as dampening terms [18] and get these equations:

$$\left\langle \frac{\partial u}{\partial t} \right\rangle = \Omega_R \sin(\phi_{MW}) \langle w \rangle + \delta \langle v \rangle - \frac{\delta \langle u \rangle}{T_2} \quad (2.16)$$

$$\left\langle \frac{\partial v}{\partial t} \right\rangle = -\delta \langle u \rangle + \Omega_R \cos(\phi_{MW}) \langle w \rangle - \frac{\delta \langle v \rangle}{T_2} \quad (2.17)$$

$$\left\langle \frac{\partial w}{\partial t} \right\rangle = -\Omega_R \cos(\phi_{MW}) \langle v \rangle - \Omega_R \sin(\phi_{MW}) \langle u \rangle - \frac{\langle w \rangle - w_0}{T_1} \quad (2.18)$$

Here, $\delta = \omega - \omega_0$ is the detuning between the present electromagnetic field and the resonance frequency of the system. $\Omega_R = \mu B_0 \hbar$ is the Rabi frequency and ϕ is the phase of the field driving the transition. T_1 is the population relaxation time and T_2 the coherence relaxation time. These equations describe the dynamics of our two-level system in the presence of the laser beams.

The quantities u , v represent the coherence of the state and w is the population in the upper or lower state. They are also the three components of the Bloch vector. It serves to visualize the temporal evolution of the state on the Bloch sphere, see fig. 2.5:

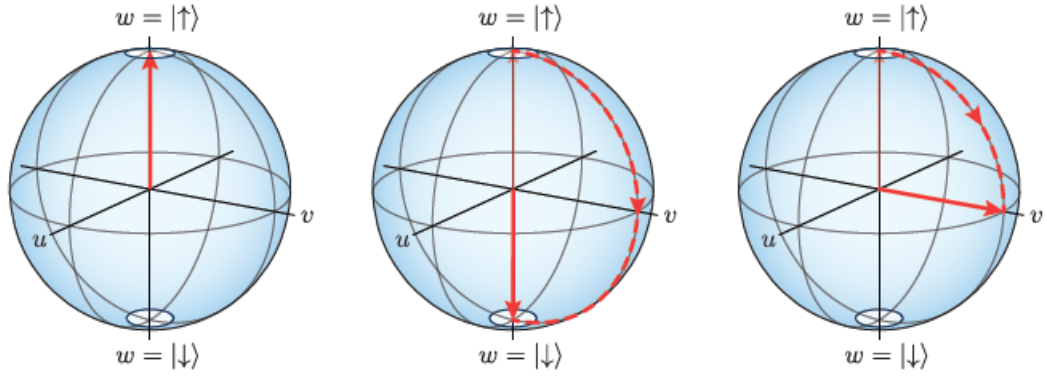


Figure 2.5: In the first picture, on the left, the atom is completely in the $|\uparrow\rangle$ state. The middle picture shows a transfer to the $|\downarrow\rangle$ state via a π -pulse and the picture on the right the transfer to the superposition state, the equatorial plane on the Bloch sphere via a $\pi/2$ pulse. [14]

The Bloch vector is related to the wave function in equation 2.15 through the state density matrix ρ :

$$w = \rho_{00} - \rho_{11}, \quad u = \rho_{10} + \rho_{01}, \quad v = i(\rho_{01} - \rho_{10}) \quad (2.19)$$

We can greatly simplify the Bloch equations by assuming the system is driven on resonance, with the detuning $\delta = 0$, without a phase difference and without any decoherence. In that case, we get this expression for the time dependence of the population:

$$w(t) = -\cos(\Omega_R(t)t) \quad (2.20)$$

From this equation, we can readily see that any given population state can be generated by applying the proper pulse. In our case, the intensity of the two laser beams providing the Raman transitions will determine the Rabi frequency, and with the pulse length t , we can create any superposition state we wish. Choosing, for example, a π -pulse with $\int \Omega_R(t)t = \pi$ will flip the population from $|\uparrow\rangle$ to $|\downarrow\rangle$. Since we can also control the phase of the driving pulse in ϕ , we can choose the rotation axis of the Bloch vector, which will be used for Ramsey Interferometry, explained in the next chapter.

2.3 Ramsey interferometry

Ramsey interferometry was pioneered by Norman Ramsey as a method to improve on the measurement techniques used to determine atomic transition frequencies, see [24]. Rabi measured the transition frequency ω_0 between the ground and excited states of an atom sample by exposing it to an oscillating field B_\perp for the duration of the atom's passage with the velocity v through an interaction zone of length L ($L/v = \tau$). Applying the field causes Rabi oscillations between the two states at a frequency Ω_\perp . The transition probability is described by a function $\propto 1/\sin^2$, which reaches its maximum, if $\Omega_\perp \tau = \pi$, this is called a π -pulse. The precision of this measurement is limited by the fact that a sample of atoms will have a certain velocity distribution and thus different amounts of time spent in the interaction zone. Also, inhomogeneities in the magnetic field can cause a broadening of the central peak of the probability distribution and further reduce the precision.

Ramsey improved on that by splitting the interaction zone into two parts, in each of which a $\pi/2$ -pulse

is applied. Between them is a propagation zone during which no oscillating field is applied. Because there is no additional field between the two interaction zones, the non-interaction zone can be made much longer than the interaction zones. The fact that the pulse-time is so short leads to a much improved precision.

Using the representation on the Bloch sphere, the sequence then is as follows. First, a $\pi/2$ pulse is applied, the atom is flipped by 90° on the Bloch sphere. Then follows the so called Ramsey-time, in which the Bloch vector is allowed to precess around the equator. The second $\pi/2$ pulse again flips the Bloch vector by 90° in a direction depending on the phase difference between the two pulses.

After the second pulse, the population in the upper state is measured. The probability to find an atom in this state is described by the so called Ramsey fringes.

2.3.1 Measurement of coherence relaxation time

As a method in our lab and many other cold atom experiments [25], Ramsey interferometry is employed in determining the coherence time, T_2 time, of the atoms in our lattice. Since we are able to control the phase of the microwave pulse that is applied to the atoms, we use this phase to scan the Ramsey fringe in the following manner. First, the atoms are prepared in the $|\uparrow\rangle$ state, then the first $\pi/2$ -pulse is applied. It transfers the atoms into an equal superposition state of $|\uparrow\rangle$ and $|\downarrow\rangle$, where it stays for a preset time Δt , the Ramsey time. Then the second $\pi/2$ pulse is applied. Using the push-out technique, we then transfer all atoms into either the $|\uparrow\rangle$ or the $|\downarrow\rangle$ state, and the former is removed from the lattice. We then measure the amount of atoms in the $|\downarrow\rangle$ state. In case of perfect resonance, if the phase difference between the two pulses is 0, all atoms are expected to be in the $|\downarrow\rangle$ state. Scanning the phase from $0-2\pi$ allows us now to observe an entire Ramsey fringe, see figure 2.6, and extract the contrast between $|\uparrow\rangle$ and $|\downarrow\rangle$. Performing this measurement for a number of Ramsey times will give us a curve as in fig 2.7, from which we can calculate the coherence time T_2 using the model introduced in Kuhr et al. [26]. In figure 2.7, we see such a T_2 time measurement, with the fit returning a result of $T_2 = 240 \pm 20 \mu\text{s}$.

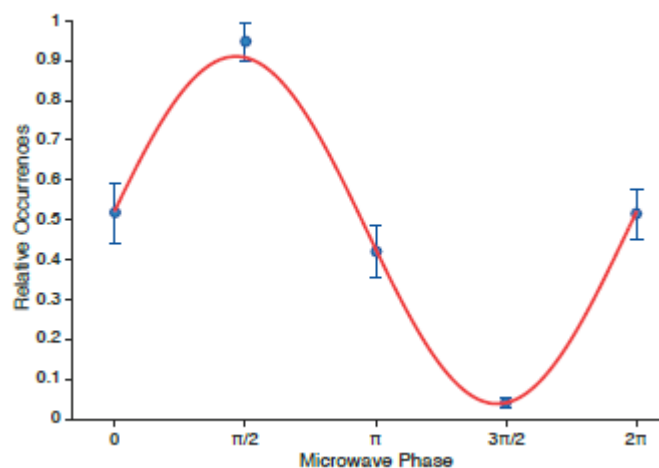
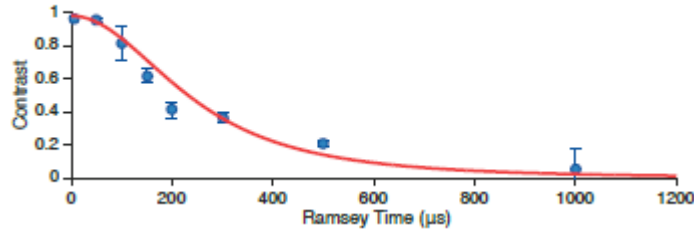


Figure 2.6: Ramsey fringe for $\Delta t = 50 \mu\text{s}$ [14]

Figure 2.7: Coherence time measurement for $T_2 = 240 \pm 20 \mu\text{s}$ [14]

2.4 Quantum speed limit

Motivated by the Heisenberg uncertainty relation, especially the somewhat undefined nature of the energy-time relation, a century of research has produced new insights into how quickly quantum systems can evolve. Realizing that Heisenberg's formulation is not an expression for a simultaneous measurement, but for an intrinsic time scale of unitary quantum dynamics [27], Mandelstam and Tamm developed the concept of the quantum speed limit. Their expression can be derived, starting from the general uncertainty relation using the Cauchy-Schwarz inequality:

$$\Delta A \Delta B \geq \frac{1}{2} |\langle [A, B] \rangle| \quad (2.21)$$

with $X = A, B$ as any quantum operator, $\Delta X = \sqrt{\langle X^2 \rangle - \langle X \rangle^2}$ and $\langle X \rangle = \langle \psi | X | \psi \rangle$.

Since the evolution of any observable A under Schrödinger's dynamics is given by the Liouville-von-Neumann equation:

$$\frac{\partial A}{\partial t} = \frac{i}{\hbar} [H, A] \quad (2.22)$$

So with $B = H$, the Hamiltonian of the system, equation 2.21 changes to:

$$\Delta H \Delta A \geq \frac{\hbar}{2} \left| \left\langle \frac{\partial A}{\partial t} \right\rangle \right| \quad (2.23)$$

We simplify this expression by choosing A to be the projector on the initial state $|\psi(0)\rangle$, which after integration yields:

$$\frac{1}{\hbar} \Delta H t \geq \frac{\pi}{2} - \arcsin \sqrt{\langle A_t \rangle} \quad (2.24)$$

Since we only wish to consider processes in which the initial and final states are orthogonal to each other, meaning $\langle \psi(0) | \psi(\tau) \rangle = 0$, we get the minimal time to evolve between the two states as:

$$\tau \geq \tau_{QSL} = \frac{\pi}{2} \frac{\hbar}{\Delta H} \quad (2.25)$$

ΔH , the variance of the Hamiltonian, is however a quite inopportune measure for timescales of quantum evolution. This is because this variance can diverge even if the average energy is finite, so the "limit", the shortest possible time in equation 2.25, can correspondingly be arbitrarily small.

As a way to overcome this problem, Margolus and Levitin derived an alternate expression, starting from the initial state $|\psi_0\rangle$ in its Eigenbasis:

$$|\psi_0\rangle = \sum_n c_n |E_n\rangle \quad (2.26)$$

For the time t , the solution for the time dependent Schrödinger equation can be similarly expanded:

$$|\psi_t\rangle = \sum_n \exp\left(-i\frac{E_n t}{\hbar}\right) |E_n\rangle \quad (2.27)$$

Now we overlap this with the initial state and estimate the quantum speed limit from the real part of this overlap:

$$S(t) = \langle\psi_0|\psi_t\rangle = \sum_n |c_n|^2 \exp\left(-i\frac{E_n t}{\hbar}\right) \quad (2.28)$$

$$\Re(S) = \sum_n |c_n|^2 \cos\left(\frac{E_n t}{\hbar}\right) \quad (2.29)$$

$$\geq \sum_n |c_n| \left[1 - \frac{2}{\pi} \left(\frac{E_n t}{\hbar} + \sin\left(\frac{E_n t}{\hbar}\right)\right)\right] \quad (2.30)$$

$$= 1 - \frac{2}{\pi} \frac{\langle H \rangle}{\hbar} t + \frac{2}{\pi} \Im(S) \quad (2.31)$$

This includes the use of a trigonometric identity: $\cos(x) \geq 1 - 2/\pi(x + \sin(x))$. Since we treat initial and final states, which are orthogonal, we have $S(\tau) = 0$ in these cases. This leads to the quantum speed limit as the minimal time for a system to evolve between two such states:

$$\tau \geq \tau_{QSL} = \frac{\pi}{2} \frac{\hbar}{\langle H \rangle} \quad (2.32)$$

With the derivations from Mandelstam and Tamm, as well as Margolus and Levitin, we are in the rather strange situation that there are two independent and different limits, which both treat the same quantum situation. They were individually verified, and Levitin and Toffoli could later show that the unified bound in equation 2.33 is tight[28]:

$$\tau_{QSL} = \max\left\{\frac{\pi}{2} \frac{\hbar}{\Delta H}, \frac{\pi}{2} \frac{\hbar}{\langle H \rangle}\right\} \quad (2.33)$$

Equation 2.33 defines the fastest attainable time-scale over which a quantum system can evolve. The limit translates to a number of applications. It defines, among other things, the maximal rates of quantum information processing and communication as well as quantum entropy production [27]. To investigate this boundary, we use Ramsey interferometry, the exact sequence for this specialized measurement will be explained in chapter 4.

Raman laser setup

In this chapter, I will cover the idea behind the modification of the previous Raman setup, the theory of Raman transitions as a tool in our experiment and the goals of the improvement.

For earlier Ramsey interferometry experiments, we used a microwave pulse to apply the $\pi/2$ pulses and changed the relative phase between the two pulses by directly changing the setting on a microwave generator [14]. This resulted in Rabi frequencies of around 56kHz. It also meant that because of the pulse length, decoherence effects influenced our measurement precision.

Now, the idea was to use an optical frequency for the pulses, seeing that, through the stronger coupling to the $D2$ line of Caesium, the Rabi frequency would be greatly increased. Consequently, the expected pulse length t , for example for a $\pi/2$ -pulse, would be shorter:

$$\frac{\pi}{2} = \int_t \Omega_R t' dt' \quad (3.1)$$

For that purpose we modified the existing Raman setup, which was used for Raman sideband cooling [14], to also accommodate interferometric applications.

3.1 Raman transitions

To realize stimulated Raman transitions, we use our setup of two home-built diode lasers at around 852nm, detuned from each other by 9.2GHz. To understand the process, we consider a simple Λ -scheme as seen in figure 3.1.

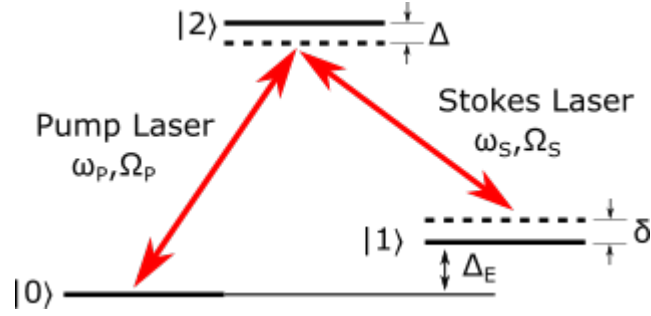


Figure 3.1: Lambda level scheme for Raman transitions

The goal is to coherently drive Rabi oscillations between states $|0\rangle$ and $|1\rangle$, separated by the energy difference ΔE . We use two lasers called the Pump laser with ω_P and Rabi frequency Ω_P and the Stokes laser with ω_S and Ω_S . Both of them couple one of the two states to an intermediate state $|2\rangle$, but are detuned from it by the detuning Δ . Through this detuning we can neglect one-photon transitions to the intermediate state. We describe the detuning of the difference of the two lasers to the two-photon resonance frequency as δ . We choose the magnitudes of these values so that Δ is larger than δ and also far larger than the Rabi frequencies.

To calculate the system's dynamics and determine expressions for the Rabi frequency and the light shift, we solve the time dependent Schrödinger equation for the Hamiltonian of the system. Using the well known rotating wave approximation and setting the energy value of $|0\rangle$ to zero, the Hamiltonian in the basis of the 3 states $|0\rangle, |1\rangle, |2\rangle$ is given as:

$$\hat{H} = \frac{\hbar}{2} \begin{pmatrix} 0 & 0 & \Omega_P \\ 0 & -2\delta & \Omega_S \\ \Omega_P & \Omega_S & -2\Delta \end{pmatrix} \quad (3.2)$$

The two Rabi frequencies $\Omega_{P,S}$ are defined by $E_0(r_o)$, the field amplitude at the position of the atom and the dipole transition operator \hat{D} :

$$\Omega_{P,,S} = -\frac{1}{\hbar} \langle e | \hat{D} \Omega_{P,S}(r_o) | g \rangle \quad (3.3)$$

where we use the indexes P and S to differentiate between the Rabi frequencies of the Pump and Stokes lasers.

We define the time dependent state of the 3-level atom as $\Psi(t)$ and express it as a superposition of the individual state weighed by their probability amplitudes C_i .

$$\Psi(t) = C_0(t)|0\rangle + C_1(t)|1\rangle + C_2(t)|2\rangle \quad (3.4)$$

Solving the time-dependent Schrödinger equation then gives us a set of three coupled differential equations for the probability amplitudes C_i :

$$i\dot{C}_0(t) = \frac{1}{2}\Omega_P C_2(t) \quad (3.5)$$

$$i\dot{C}_1(t) = \frac{1}{2}\Omega_S C_2(t) - \delta C_1(t) \quad (3.6)$$

$$i\dot{C}_2(t) = \frac{1}{2}(\Omega_P C_0(t) + \Omega_S C_1(t)) - \Delta C_2(t) \quad (3.7)$$

Earlier we defined Δ to be much larger than the Rabi frequencies, so we see from the third equation that $|2\rangle$ will show a much faster oscillating behaviour than $|0\rangle$ and $|1\rangle$. That means \dot{C}_2 will average out to 0 over many oscillation cycles, we can disregard it and gain an effective two level-system:

$$i\dot{C}_0(t) = \frac{\Omega_P}{4\Delta}(\Omega_P C_0(t) + \Omega_S C_1(t)) \quad (3.8)$$

$$i\dot{C}_1(t) = \frac{\Omega_S}{4\Delta}(\Omega_P C_0(t) + \Omega_S C_1(t)) - \delta C_1(t) \quad (3.9)$$

For which we can calculate the effective Hamiltonian as:

$$\hat{H}_{\text{eff}} = \frac{\hbar}{4} \begin{pmatrix} \frac{\Omega_P^2}{\Delta} & \frac{\Omega_P \Omega_S}{\Delta} \\ \frac{\Omega_P \Omega_S}{\Delta} & \frac{\Omega_S^2}{\Delta} - 4\delta \end{pmatrix} \quad (3.10)$$

We can calculate the energy shift Λ_i of the states $|0\rangle$ and $|1\rangle$ from the diagonal terms, which increases or lowers the energy, depending on the detuning:

$$\Lambda_0 = \hbar \frac{\Omega_P^2}{4\Delta}, \quad \Lambda_1 = \hbar \frac{\Omega_S^2}{4\Delta} \quad (3.11)$$

This is known as the AC-stark shift, also simply called light-shift due to the fact that they are caused in the interaction of the atom state with light. Since both states are affected, we can calculate an effective differential light shift as:

$$\delta_\Lambda = \Lambda_1 - \Lambda_0 \quad (3.12)$$

with the effective two-photon Raman detuning then being:

$$\delta_{\text{eff}} = \delta - \delta_\Lambda \quad (3.13)$$

From the off-diagonal terms, which represent the coupling between the two states, we calculate the two-photon Rabi frequency:

$$\Omega_R = \frac{\Omega_P \Omega_S}{\Delta} \quad (3.14)$$

With that and the generalized Rabi frequency $\Omega_0 = \sqrt{\Omega_R^2 - \delta_{\text{eff}}^2}$ we solve the Schrödinger equation for the effective Hamiltonian. It yields the time dependent population densities of the two states, calculated under the assumption that the initial population was in state $|0\rangle$:

$$\rho_0(t) = |C_0(t)|^2 = 1 + \frac{\Omega_R^2}{2\Omega_0^2} [\cos(\Omega_0 t) - 1] \quad (3.15)$$

$$\rho_1(t) = |C_1(t)|^2 = \frac{\Omega_R^2}{2\Omega_0^2} [1 - \cos(\Omega_0 t)] \quad (3.16)$$

As can be seen in fig 3.2, a full population inversion is only achieved for $\delta_{\text{eff}} = 0$. This means we require the two lasers to operate with minimal frequency fluctuations at the resonance frequency.

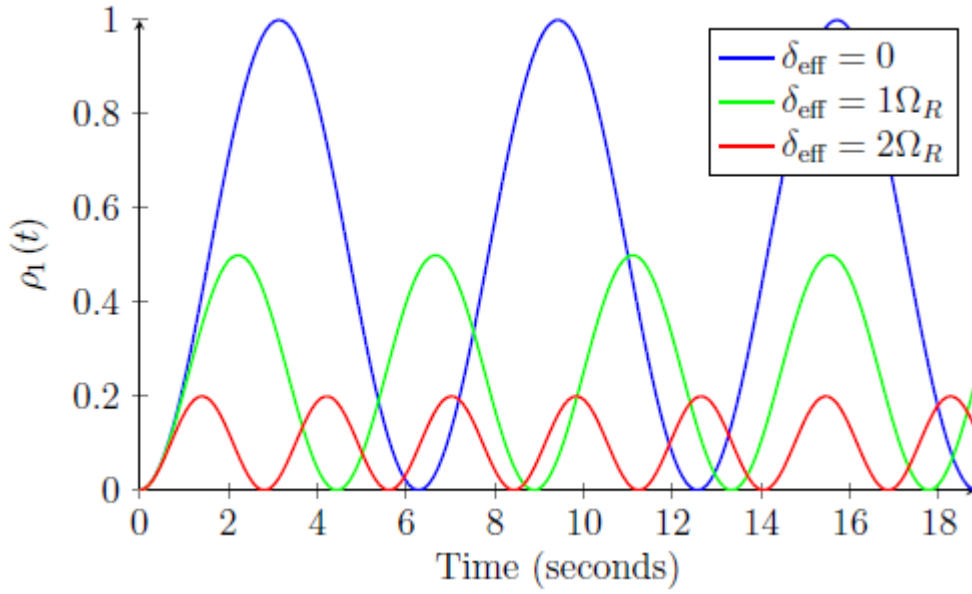


Figure 3.2: Rabi oscillations depending on the two photon Raman detuning δ_{eff} [29]

Cross coupling In calculating the Rabi frequency, there is an effect we disregarded. While the Pump and Stokes lasers are meant to only be coupling their respective state to state $|2\rangle$ with detuning Δ , they also couple the other state to state $|2\rangle$. In case of the Stokes laser with detuning $\Delta - \Delta_E$, for the Pump laser with detuning $\Delta + \Delta_E$, see fig 3.3.

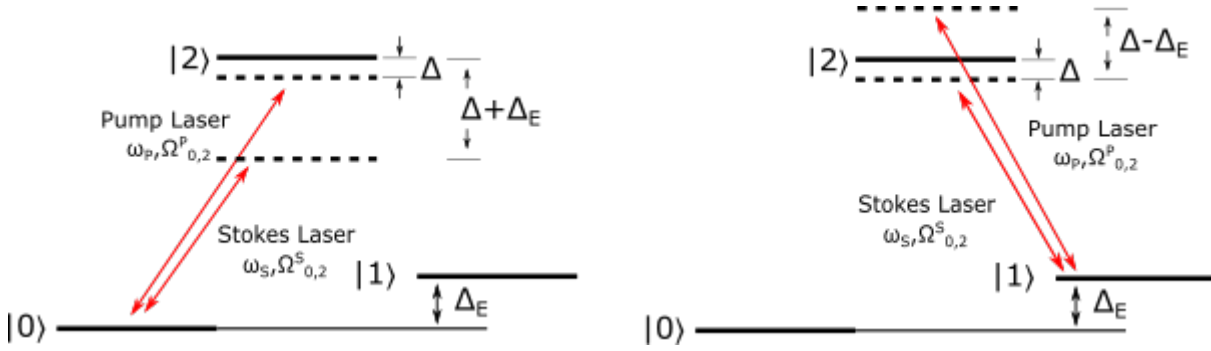


Figure 3.3: Cross coupling of the Pump and Stokes beams

In our experiment, Δ is larger than Δ_E , so this cross coupling will not cause any additional one- or two-photon transitions and therefore not affect the Rabi frequency, but it will have an effect on the light shift. The light shift of a ground state then becomes:

$$\Lambda_g = \Lambda_g^P + \Lambda_g^S \quad (3.17)$$

so that the light shifts for our two states $|0\rangle$ and $|1\rangle$ becomes:

$$\Lambda_0 = \frac{\hbar}{4} \left[\frac{(\Omega_{0,2}^P)^2}{\Delta} + \frac{(\Omega_{0,2}^S)^2}{\Delta - \Delta_E} \right] \quad (3.18)$$

$$\Lambda_1 = \frac{\hbar}{4} \left[\frac{(\Omega_{1,2}^S)^2}{\Delta} + \frac{(\Omega_{1,2}^P)^2}{\Delta + \Delta_E} \right] \quad (3.19)$$

3.2 Raman transitions in Caesium

Applying these principles to affect our qubit in the manner described in chapter 2 presented some challenges. For the purpose of Raman sideband cooling, the two laser beams were arranged in a way that one of them, the slave beam, would enter the vacuum chamber in lattice direction, σ_+ -polarized. While the other, the master beam, was directed towards the atoms from above, the z -direction, together with the MOT- z -beam. It is circularly polarized as well, but due to the angle of incidence induces both π and σ_{\pm} transitions. The reason for this orientation is that in order to perform the cooling, the laser beams need to radially transfer momentum to the atoms. That means the beams cannot be copropagating and an angle between them is required.

This setup was unsuitable for us since the z -beam was not well focused, quite wide, and that would have resulted in a relatively low intensity experienced by the atoms and consequently a low Rabi frequency. The solution was to direct both Raman beams along the lattice, because in our case, copropagation was not a problem, since both beams will traverse the same focusing optics as the lattice beams. Since now the two beams were no longer able to induce π -transitions, driving our original qubit transition without a large loss of power was no longer an option. We changed our qubit from the initial setup with $|F = 3, m_F = 3\rangle$ and $|F = 4, m_F = 4\rangle$ to $|F = 3, m_F = 3\rangle$ and $|F = 4, m_F = 3\rangle$. This meant atom initialization would now happen in the $|F = 3, m_F = 3\rangle$ state, which is connected to the dark state of the optical pumping through a microwave transition.

This also had some implications for the possible combinations of polarizations of the Raman beams. Following [30], we see that the Rabi frequency of the two-photon process is changed by a factor, depending on the initial hyperfine sublevel and the polarization combination of the two laser beams:

$$\Omega_{R,0} = \Omega_R \sqrt{X(m_F)} = \frac{\Omega_P \Omega_S}{2\Delta} \sqrt{X(m_F)} \quad (3.20)$$

$$X(m_F) = \begin{cases} \frac{1}{288}(4+m_F)(5+m_F) & \text{in case of: } (\pi, \sigma_-), (\sigma_+, \pi) \\ \frac{1}{288}(4-m_F)(5-m_F) & \text{in case of: } (\pi, \sigma_+), (\sigma_-, \pi) \\ \frac{1}{9}(1 - (\frac{m_F}{4})^2) & \text{in case of: } (\sigma_+, \sigma_+), (\sigma_-, \sigma_-) \\ 0 & \text{in case of: } (\pi, \pi), (\sigma_\pm, \sigma_\mp) \end{cases} \quad (3.21)$$

If the two Raman beams now had opposite circular polarizations, we can see that the transition would be completely suppressed. So we chose the σ_+ -polarization for both of the beams and overlapped the beams with the according component of the synthesized arm of the optical lattice.

3.3 Optical setup

The existing Raman setup consisted of 2 home-made diode lasers at a wavelength of around 852nm, the $D2$ line of Caesium and the supporting optics. Since they were directed at the experiment separately, the optical layout had to be changed, but the temperature and current settings could be kept at similar levels, after verifying that they were detuned from each other by 9.2GHz, which is the hyperfine splitting between the $|F=3\rangle$ and $|F=4\rangle$ states. The detuning from the $D2$ line itself, to avoid one-photon transitions, is around 238GHz. See figure 3.4

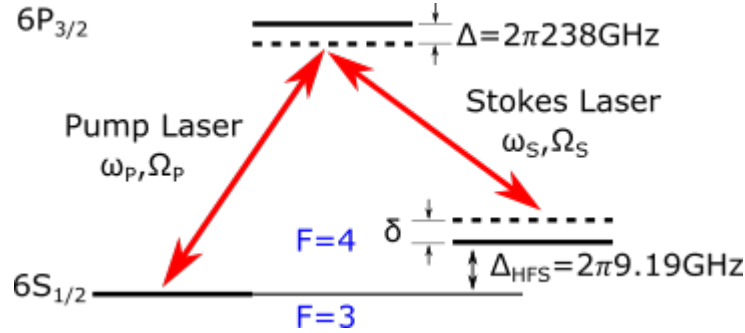


Figure 3.4: Laser settings and Caesium level scheme of Raman setup

We needed to divert enough optical power to be able to observe Rabi oscillations while still being able to do the sideband cooling. Since sideband cooling only requires very little, however, almost the entire power of the two lasers could be used for the new setup. Reaching high enough Rabi frequencies with the available power was questionable though. We made plans to boost the laser power with a tapered amplifier, which would yield up to 1 – 2W per beam. Ultimately these plans were not executed due to space constraints and because we were able to reach high enough power levels at the position of the atoms. But this is still a possible avenue of improvement in later experiments, if more power is

required. Fig. 3.5 shows the optical components:

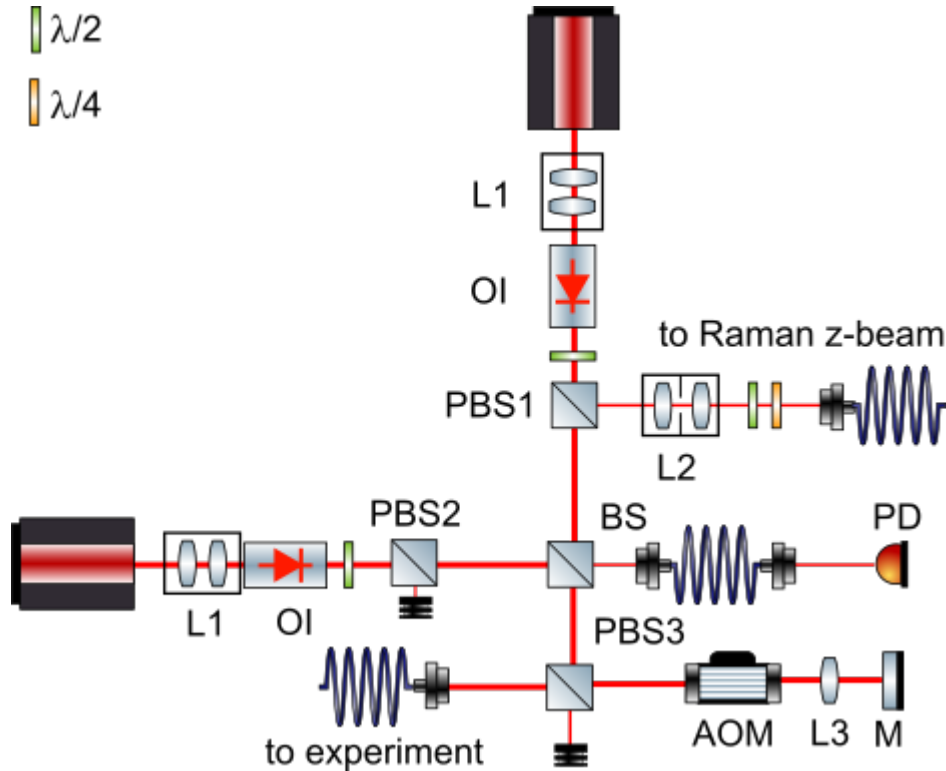


Figure 3.5: Optical components of the Raman setup

Both lasers start at around 50mW of power at their output and are first directed through a beam-shaping telescope (L1) of cylindrical lenses. Two optical isolators protect the lasers from reflections that could damage the cavities. After that, the polarization of both beams is rotated by a $\lambda/2$ plate, so we can control the amount of power passing the outputs of the following polarizing beamsplitters (PBS 1&2). Here, the master beam is split, so a fraction of it can continue towards the experiment as the z -beam for the Raman sideband cooling and the remaining power is directed towards a second beam splitter (BS), non-polarizing this time, where it is combined with the beam from the slave laser. The slave beam is split, so we can control the amount of power passing through and being combined in the following beam splitter with the master beam. The discarded power is directed to a beam dump. The non-polarizing beam splitter evenly splits the combined power of both beams. The first arm directs the light towards an optical fiber and a photo diode (PD) which belongs to the optical phase lock loop, explained later in this section. The second arm leads to the AOM. Before reaching the AOM, the beams are directed through a beam-shrinking telescope, with lenses of 150mm and -50 mm focal lengths, which is necessary to avoid clipping at the aperture of the AOM. That way we achieve a higher efficiency in the AOM throughput.

3.3.1 AOM in double pass configuration

As mentioned at the beginning of this chapter, we want to take advantage of the shorter pulse length of a $\pi/2$ -pulse due to the higher Rabi frequency. However, pulses of durations in the sub- μs -regime cannot be precisely done with mechanical shutters. Ideally, we want to be able to realize pulse lengths down to around 100ns, so an AOM suits our needs perfectly. The model we chose has its maximum efficiency at 80MHz.

To produce the pulses, the AOM is set up in double pass configuration [31] as seen in fig 3.6. The combined beams from the master and slave lasers pass a polarizing beam splitter and enter the AOM from the left side. With the AOM turned off, only the 0th order of the beam is seen. Additional orders appear on either side of the 0th order, once the AOM starts operation. We optimize the transmission of the AOM for the 1st order beam and block all other orders.

For the second pass we prepare a lens (L3) and mirror (M) in cat's eye configuration [32]. The mirror is placed at the focal point of the lens and the incoming 1st order beam is reflected as seen in figure 3.6. Like in the first pass through the AOM, the 0th order beam is blocked and the remaining beam, the 1st order in second pass -since after passing through the AOM its polarization is flipped- can pass through the beam splitter and towards the following optics.

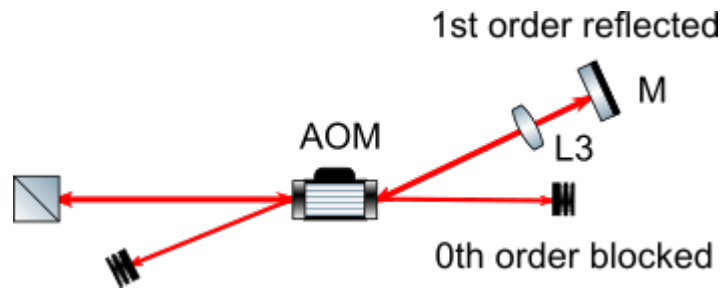


Figure 3.6: AOM in double pass configuration

The advantage of the double pass is the high suppression ratio of up to 10^{-5} . Effectively, since we couple into an optical fiber after the AOM, when we direct the light towards the atoms, we gain a suppression ratio of up to 10^{-6} at the position of the atoms.

3.3.2 Control circuitry of the AOM

To control the AOM, we installed a number of control electronics, seen in the schematic circuit diagram fig 3.7:

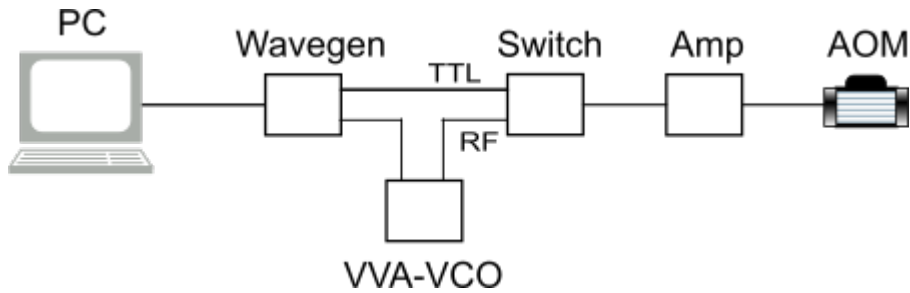


Figure 3.7: Schematic control circuit for the AOM; Amplifier: Mini Circuits (MC) ZHL-1-2W-S+, VCO: MC ZX95-78+, VVA: MC ZX73-2500+, Switch: MC ZASWA-2-50DRA+, Wavegen: Agilent 33522A

We program the pulse length and amplitude from the PC into the wavegen, which has two outputs. The first one is a TTL pulse, which is the logic signal for the switch. The second output provides the information for the VVA-VCO-circuit. It contains the information to produce a pulse of a defined duration and amplitude.

The RF output from this circuit is the input for the switch, which gets passed on, if there is a positive logic signal. The signal then reaches a gain block amplifier and from then on the AOM.

Since the AOM has different output efficiencies depending on the supplied voltage, we can control the power of the Raman pulses directly from the computer. This translates to a direct control of the induced Rabi frequencies at the desired transition.

3.3.3 Optical phase lock loop

We require a stable frequency and phase relation with minimal fluctuations between the two lasers, as variations would lead to decoherence of the Raman transitions. This is accomplished with a phase lock loop setup, as seen in figure 3.8:

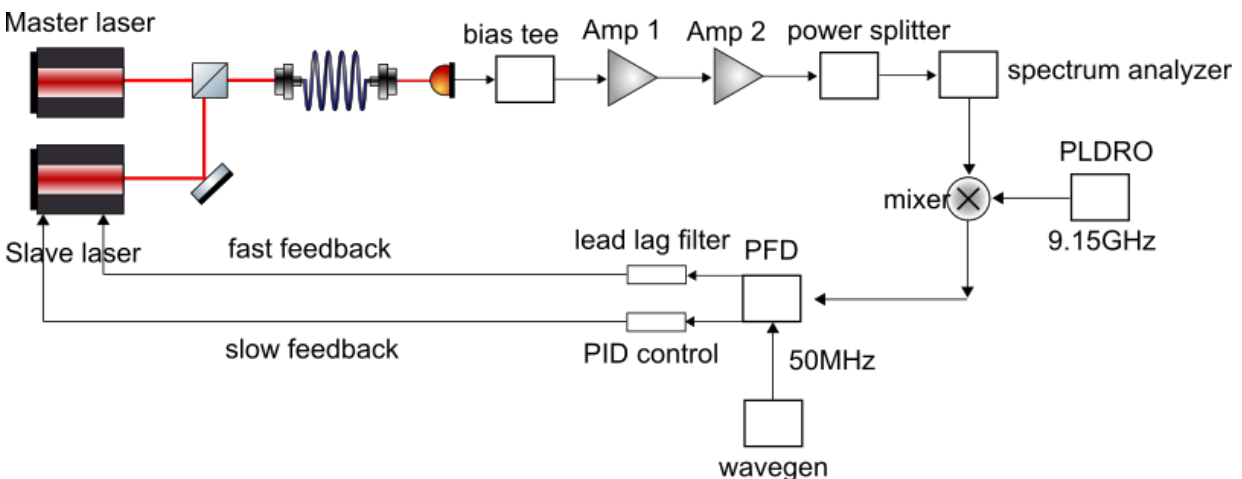


Figure 3.8: Optical phase lock loop as used in our system; Photo diode: Hamamatsu G4176-03, Bias tee: Mini-Circuits® ZX85-12G+, Amp 1: Kuhne Electronics KU LNA 922A, Amp 2: Miteq AFS5-08001200-40-10P-5, PLDRO: Resotech Inc, phase frequency detector: MC100EP140

In general, an OPLL works by comparing the phase of, in our case, two lasers, and controls the phase of one of them (called slave laser in figure 3.8) so it has a fixed phase relation to the other one (called master laser), which is free running.

On the left side of the schematic, there are the two lasers, called master and slave laser, which reach the photo diode with roughly 2mW each. A precise matching of the laser powers is not necessary as long as the photo diode is sufficiently irradiated to detect the beating signal, though they need to have the same polarization. This beating signal is a result of the two beams interfering. It is produced by two signals with different frequencies:

$$f_{\text{beat}} = |f_1 - f_2| \quad (3.22)$$

The following signal will be seen by the photo diode, where the index m signifies the master, s the slave laser:

$$\begin{aligned} I_{PD} &\propto |E_m \cos(\omega_m t + \phi_m) E_s \cos(\omega_s t + \phi_s)|^2 \\ &= |E_m|^2 \cos^2(\omega_m t + \phi_m) + |E_s|^2 \cos^2(\omega_s t + \phi_s) + 2E_m E_s \cos(\omega_m t + \phi_m) \cos(\omega_s t + \phi_s) \\ &= E_m E_s \cos((\omega_m - \omega_s)t + \phi_m - \phi_s) + E_m E_s \cos((\omega_m + \omega_s)t + \phi_m + \phi_s) \\ &\quad + |E_m|^2 \cos^2(\omega_m t + \phi_m) + |E_s|^2 \cos^2(\omega_s t + \phi_s) \end{aligned}$$

It can be seen that there is a term proportional to the sum of the two frequencies and one proportional to the difference. We select for the term proportional to $\cos((\omega_m - \omega_s)t + \phi_m - \phi_s)$, the beating signal. This signal is then mixed with a reference frequency from a local oscillator (LO) to create an error signal proportional to the phase difference $\phi_m - \phi_s$. In this mixing, we once again get a signal proportional to the sum of the two frequencies and one proportional to the difference. A low-pass filter suppresses the sum contribution and the remaining error signal then looks as follows:

$$E(t) \propto \cos((\omega_m - \omega_s - \omega_{LO})t + \phi_m - \phi_s - \phi_{LO}) \quad (3.23)$$

In case the frequency difference between the two beams is the same as ω_{LO} , this expression will only depend on the phases. Since the phase of the local oscillator can be chosen arbitrarily, we set it to be $\pi/2$ and the expression becomes:

$$E(t) \propto \sin(\phi_m - \phi_s) \quad (3.24)$$

To minimize this value, the servo loop is closed by feeding this error signal back to the laser.

Going back to figure 3.8, we continue with the electronics. The first element is a bias tee, which determines the set point of the photo diode, in order to continue with a better signal to noise ratio. The beating signal is then amplified by two amplifiers and mixed with the signal from the PLDRO (Phase Locked Dielectric Resonator Oscillator), which gives out a frequency of 9.15GHz. Two signals are created, one whose frequency is the sum of the frequencies of the two signals and one whose frequency is their difference. The summed up frequency is filtered out due to the limited bandwidth of the electronics, so we continue only with the so-called mixed down frequency.

In the next step, a phase frequency discriminator compares the mixed down beat signal with a reference signal from the wavegenerator and returns an error signal. The advantage of using a PFD instead of

directly mixing the two signals is that the error signal is directly proportional to the phase difference and not only in first order approximation. Also, in case the frequencies of the two signals are different, which would lead to the phase error increasing rapidly, the PFD provides an additional error signal, depending on the frequency. This frequency will usually be around 50MHz, the difference between the detuning of the lasers at 9.2GHz and the output of the PLDRO at 9.15GHz, which corresponds to the transition frequency of the atom sample. Depending on variations in the sample, this may vary itself, so before each experimental run, we measure this frequency spectroscopally. In our setup it is provided by a Keysight M3300A PXIe AWG and Digitizer, which can be set to any frequency we require.

Phase and frequency of the mixed down beating signal are now regulated by the OPLL through two feedback loops, which aim to minimize the error signal. The slow feedback loop operates at a bandwidth of 1kHz and up to an amplitude of a few hundred MHz and counteracts the slow fluctuations. It does so via a piezzo-electric ceramic, controlling the grating of the external cavity slave laser through a PID servo loop. The fast feedback is provided by changing the diode current of the slave laser and covers fluctuations up to 3MHz with amplitudes of 1MHz. The fast loop also contains a lead-lag filter, designed by K.Schörner, to shape the frequency characteristics, which ensures a gain < 1 for frequencies where the total phase shift is larger than 120° .

To adjust the OPLL, we change the gain settings of the feedback PID system and monitor the beating signal on a spectrum analyzer. The observed signal is seen in figure 3.9. Both pictures show the same trace with the strong central peak at 9.195MHz in the center and the two servo bumps on either side. They are barely visible, so as a guide to the eye, the picture on the right has the marker on the right side of the central peak right atop that servo bump at 9.199MHz. Comparing the peak heights between the central frequency and the servo bumps gives us a suppression of around 65.7dBm

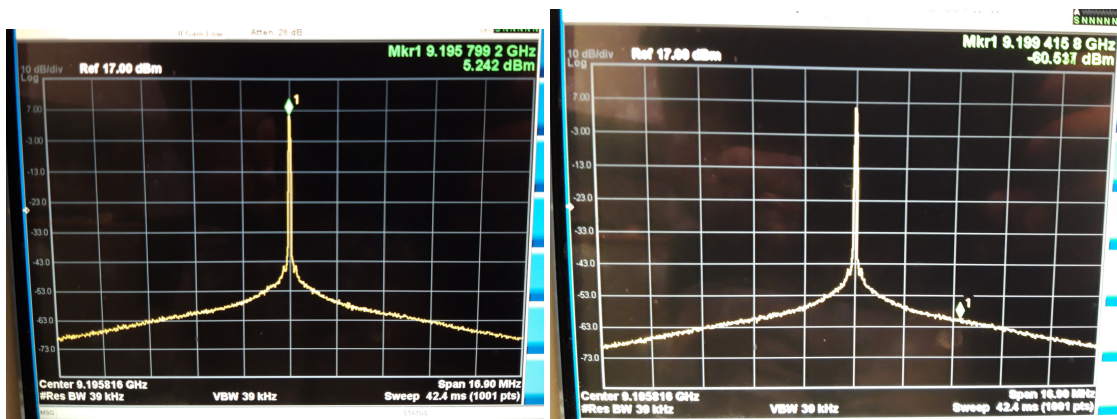


Figure 3.9: Picture of beating signal with comparison of peak heights

Beating signal linewidth

To quantify the beating signal, we also recorded the spectrum of the mixed down 50MHz beat signal with a spectrum analyzer. Here, it is controlled only by the piezzo lock. We fit it with a Voigt profile to extract the linewidth. The fit returns a Voigt linewidth of 40.9kHz.

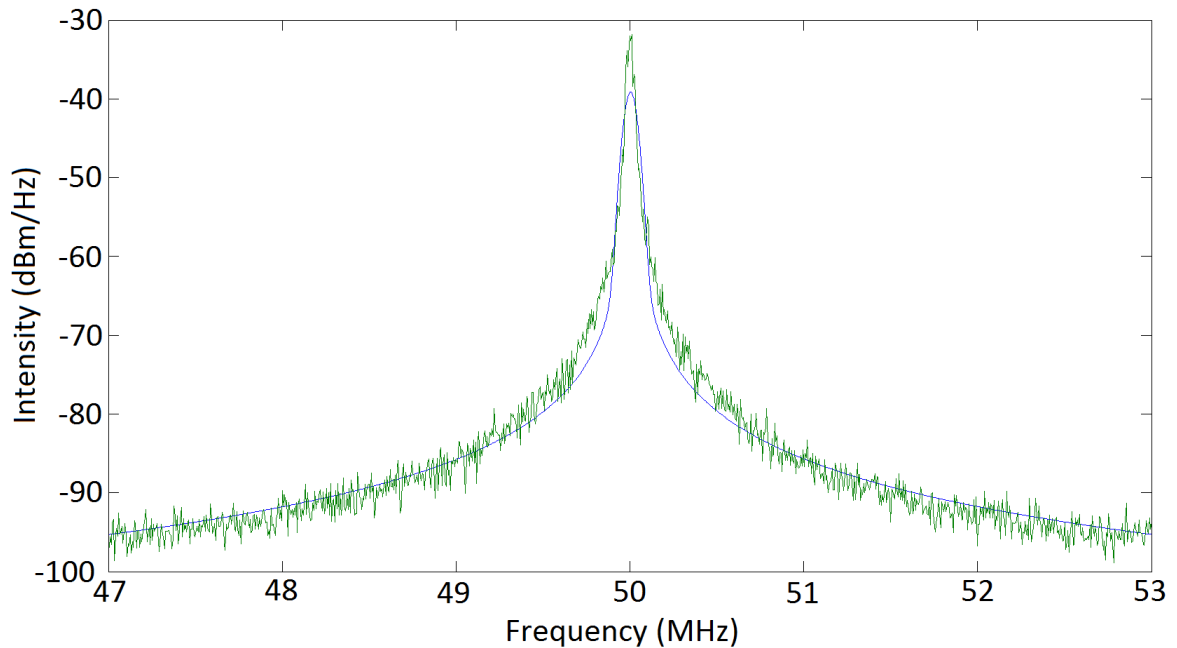


Figure 3.10: Linewidth fit of mixed down beat signal

3.3.4 Cleaning the lattice control loop

After the AOM, we direct the two beams through an optical fiber onto the experimental table. In order to achieve the best possible overlap with the optical lattice, we combine the Raman beams with one of the lattice beams themselves. Specifically, the so called DT1L beam, which is one of the two parts of the polarization synthesized arm of the lattice.

For the overlap, we cannot use a polarizing beamsplitter like in other cases. The reason is that the two components of the polarization synthesized arm of the optical lattice are of opposite linear polarizations when they are combined. We use a Wollaston prism to overlap the two components and later change their polarization to the positive and negative circular polarizations. So trying to overlap one of the two components with the Raman beams using a PBS would only lead to light being lost in the following Wollaston prism.

So we took advantage of the fact that the Raman and lattice beams have a slight difference in wavelength. Since the Raman lasers run at around 852nm and the laser for the lattice beams at 866nm, we could use a Versa Chrome Edge tunable longpass filter. This optical element acts as a high pass filter, where the edge frequency depends on the angle of incidence, see figure 3.11, the specifications from the manufacturer, where the blue trace represents a 60°AOI and the orange trace a 0°AOI.

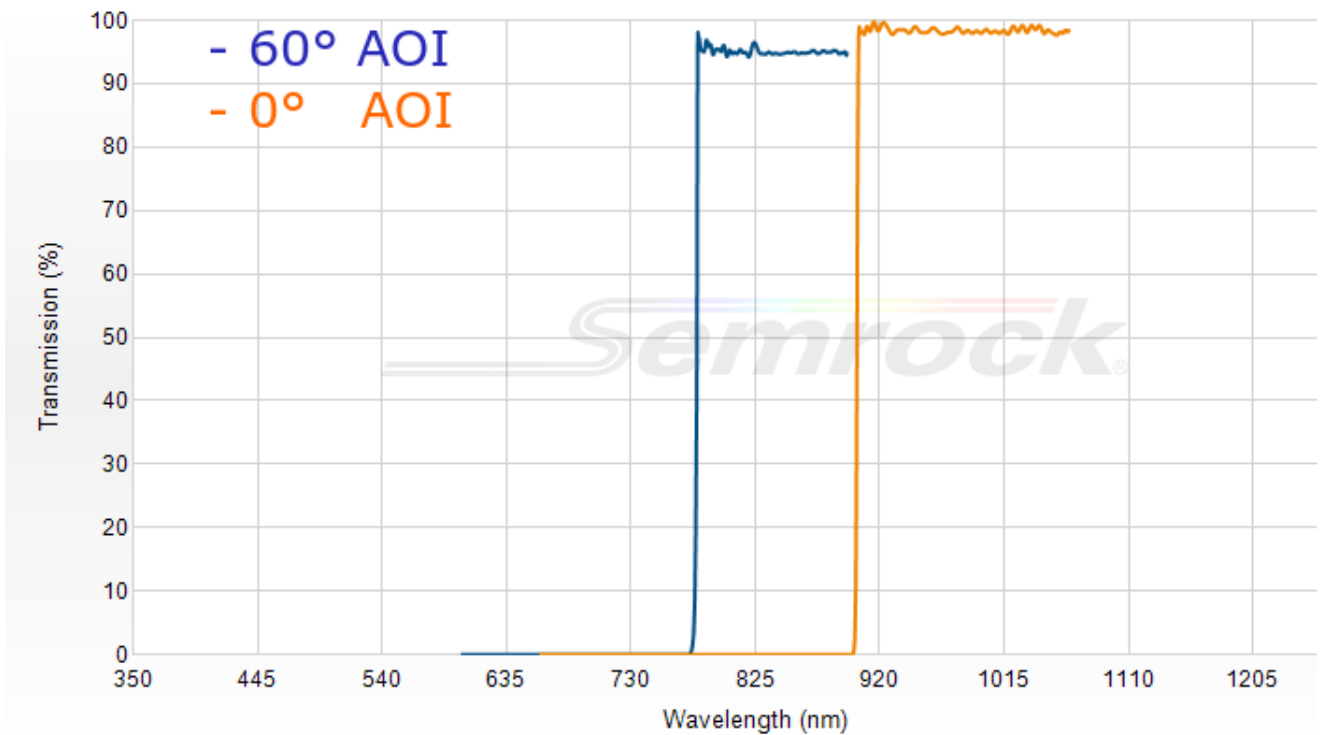


Figure 3.11: Transmission against wavelength for different angles of incidence

We overlapped the two beams using the configuration in figure 3.12.

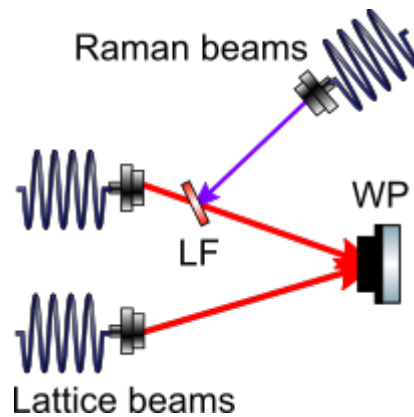


Figure 3.12: Overlap of Raman beams with DTIL beam

The problem now is that the lattice beams are themselves phase and frequency controlled. The point in the setup where a part of the light gets split off to be directed to their respective photo diodes comes a bit later, however. Having light of a different frequency as part of the beams that enter the control loops would make a stable lock impossible. So we used another of the tuneable long pass filters, cut it into four pieces, and positioned them in front of the control loops' photo diodes, see figure 3.13:

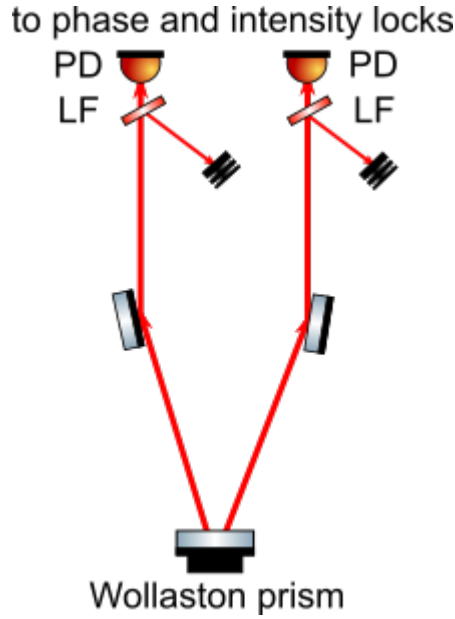


Figure 3.13: Removing Raman light before phase and intensity locks

Where earlier we used the angle dependence of the transmission to overlap two beams, we now use it to separate them. The filters were placed just so that only light from the Raman beams was reflected and directed at a beam dump, while the lattice beams were fully transmitted to enter the photo diodes.

3.4 Characterization

In order to do precise experiments, we need to be able to control our Raman pulses well. We need to make sure that the power of the beams can be adjusted with precision, that the lasers are stable and remain at set power levels, that the pulses are as long as we program them to be, and that we know our Rabi frequency well.

3.4.1 Calculation of induced light shift and Rabi frequency

To know what to expect from our system, we will first calculate several quantities that characterize it well. These calculations refer to two beams with a beam waist of $17\mu\text{m}$ at the position of the atoms, identical to that of the lattice, and 1.19mW of power per beam.

The detuning from the D2 line of Caesium:

$$\Delta_{\text{detuning}} = \frac{\omega_{D2} - \text{mean}[\omega_S\omega_P]}{2\pi} = 238.3148\text{GHz} \quad (3.25)$$

Where $\omega_{D2}, \omega_S, \omega_P$ denote the frequencies of the D2 line, the Stokes and Pump lasers respectively. As mentioned in the first chapter, a result of the interaction between light and atoms is a shift in the

energy levels, the AC-Stark shift. To calculate it, we have to add up the individual potential changes caused by the two lasers to the two levels, $F=3$ and $F=4$, which constitute our two-level system:

$$\begin{aligned}
U_{S3} &= \frac{-\pi c^2 \Gamma}{2\omega_{D2}^3} \left(\frac{2 + pg_{F_3}^3}{\omega_{D2} - \omega_S} + \frac{2 + pg_{F_3}^3}{\omega_{D2} + \omega_S} + \frac{1 - p * g_{F_3}^3}{\omega_{D1} - \omega_S} + \frac{1 - pg_{F_3}^3}{\omega_{D1} + \omega_S} \right) \frac{I}{\hbar} \\
U_{P3} &= \frac{-\pi c^2 \Gamma}{2\omega_{D2}^3} \left(\frac{2 + pg_{F_3}^3}{\omega_{D2} - \omega_P} + \frac{2 + pg_{F_3}^3}{\omega_{D2} + \omega_P} + \frac{1 - pg_{F_3}^3}{\omega_{D1} - \omega_P} + \frac{1 - pg_{F_3}^3}{\omega_{D1} + \omega_P} \right) \frac{I}{\hbar} \\
U_{S4} &= \frac{-\pi c^2 \Gamma}{2\omega_{D2}^3} \left(\frac{2 + pg_{F_4}^3}{\omega_{D2} - \omega_S} + \frac{2 + pg_{F_4}^3}{\omega_{D2} + \omega_S} + \frac{1 - pg_{F_4}^3}{\omega_{D1} - \omega_S} + \frac{1 - pg_{F_4}^3}{\omega_{D1} + \omega_S} \right) \frac{I}{\hbar} \\
U_{P4} &= \frac{-\pi c^2 \Gamma}{2\omega_{D2}^3} \left(\frac{2 + pg_{F_4}^3}{\omega_{D2} - \omega_P} + \frac{2 + pg_{F_4}^3}{\omega_{D2} + \omega_P} + \frac{1 - pg_{F_4}^3}{\omega_{D1} - \omega_P} + \frac{1 - pg_{F_4}^3}{\omega_{D1} + \omega_P} \right) \frac{I}{\hbar}
\end{aligned}$$

Where U_{S3} denotes the potential shift of the Stokes laser to the $F = 3$ state, the other cases are named accordingly. Γ is the linewidth of the D2 transition, p signifies a matrix for σ_+ -polarized light and g_{F_3} and g_{F_4} are the Lande factors of the fine structure. The resulting combined light shift is then:

$$U_{LS} = U_{S3} + U_{P3} + U_{S4} + U_{P4} = 3451.0827\text{kHz} \quad (3.26)$$

The Rabi frequency of the system under influence of the Pump and Stokes beams is calculated with:

$$\Omega_0 = \frac{1}{\hbar^2} \sqrt{7/120} \sqrt{5/24} \frac{D_{3/2}^2 I}{\epsilon_0 c \Delta} = 1.5002\text{MHz} \quad (3.27)$$

This is around 2 orders of magnitude larger than the Rabi frequencies we usually get using the microwave pulses. With that value, we can expect π -pulse durations of around $0.3333\mu\text{s}$, which is also significantly shorter than with the microwave.

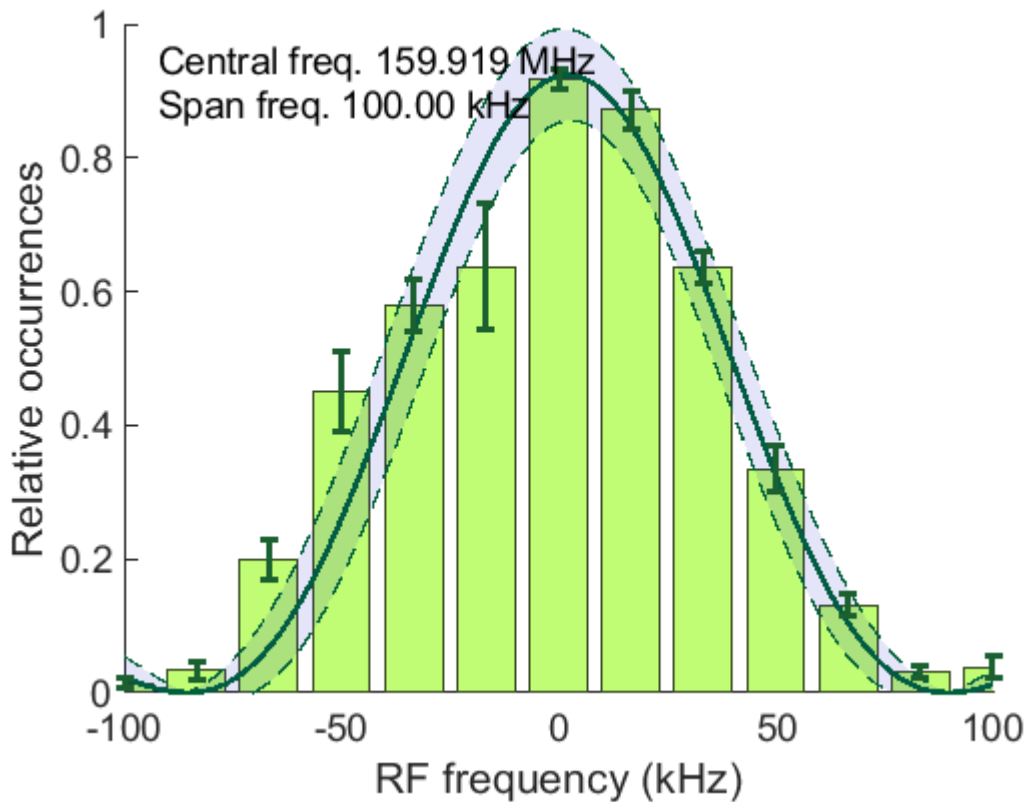
From CJ Foot's *Atomic Physics* [33] we get an estimation for the photon scattering probability of our Raman beams:

$$P_{sc} = \pi \frac{\Gamma}{\Delta} = 6.8813e - 05 \quad (3.28)$$

with a corresponding scattering rate of $R_{sc} = 5670.8534$ photons per second, where Γ is the linewidth of the D2 transition and Δ the mean detuning of the Pump and Stokes beams from that transition.

3.4.2 Light shift from Raman beams

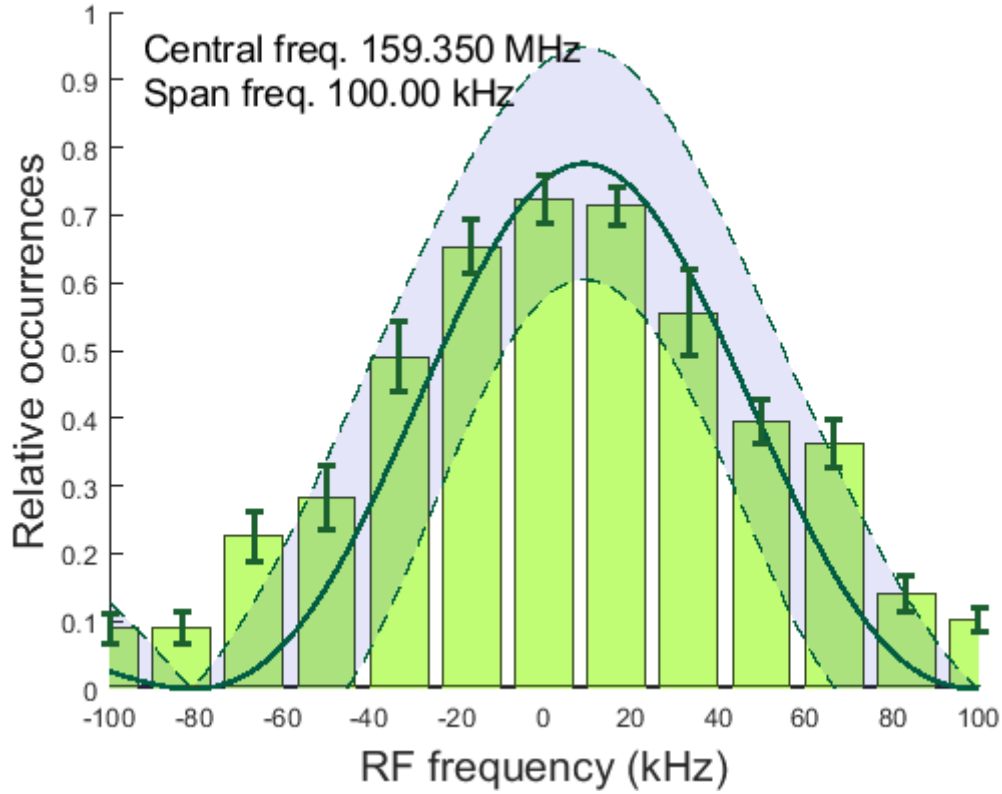
To determine the light shift the atoms experience when the Raman beams are turned on, we measure the transition frequency of our atoms. We can scan the frequency using the microwave generator, which applies multiple square pulses with changing frequencies. We first take a spectrum without the Raman beams, see figure 3.14.



$1 - \alpha$	95.0%
Reduced χ^2	6.329
Survival	1 ± 0.131
Rabi frequency[kHz]	39.523 ± 7.023
Frequency offset[kHz]	2.127 ± 1.864
Pulse duration[μ s]	10.400

Figure 3.14: Microwave spectrum to measure light shift, without Raman beams

Then another spectrum with the Raman beams on. Here we must consider what power to use. At high power levels, the spectrum will be much flatter and more spread out, because the Gaussian intensity profile will cause different light shifts for the atoms, which are spread out due to the radial temperature. This effect is more pronounced for higher powers, because the intensity profile will then cover a larger area. At full power, the peak is spread so wide that our fitting routine produced large errors. So we took the second spectrum at 0.2mW per beam, around 1/6 of the maximum, see figure 3.15.



$1 - \alpha$	95.0%
Reduced χ^2	16.394
Survival	1 ± 1.151
Rabi frequency[kHz]	32.985 ± 33.695
Frequency offset[kHz]	9.273 ± 4.847
Pulse duration[μ s]	10.400

Figure 3.15: Microwave spectrum to measure light shift, with Raman beams

From the fits we can calculate the light shift as the shift in position of the carrier. Both the central frequency and the frequency offset have to be considered, and we get:

$$U_{\text{LS}} = (f_{\text{central}}^1 + f_{\text{offset}}^1) - (f_{\text{central}}^2 + f_{\text{offset}}^2) = 561 \pm 5.193\text{kHz} \quad (3.29)$$

Where f_{central}^1 and f_{offset}^1 refer to the measurement without the Raman beams and f_{central}^2 and f_{offset}^2 to the measurement with them. Since the induced light shift scales linearly with the laser power, this matches our calculations above, which were performed assuming the full power of 1.19mW per beam.

3.4.3 Raman laser phase stability

To ascertain the quality of our OPLL, it is important to know how stable the phase state of the combined Raman lasers is. As explained in a previous chapter, we measure the beating signal between the two lasers, mix it down to 50MHz and then lock that to a 50MHz signal from a local oscillator. We determine the phase stability by mixing that beating signal with the signal from the wavegen and then measuring the phase difference and mixed signal average DC for different delays. The delays were introduced by changing the cable length piece by piece in discrete steps. The measurement yields the plot in figure 3.16.

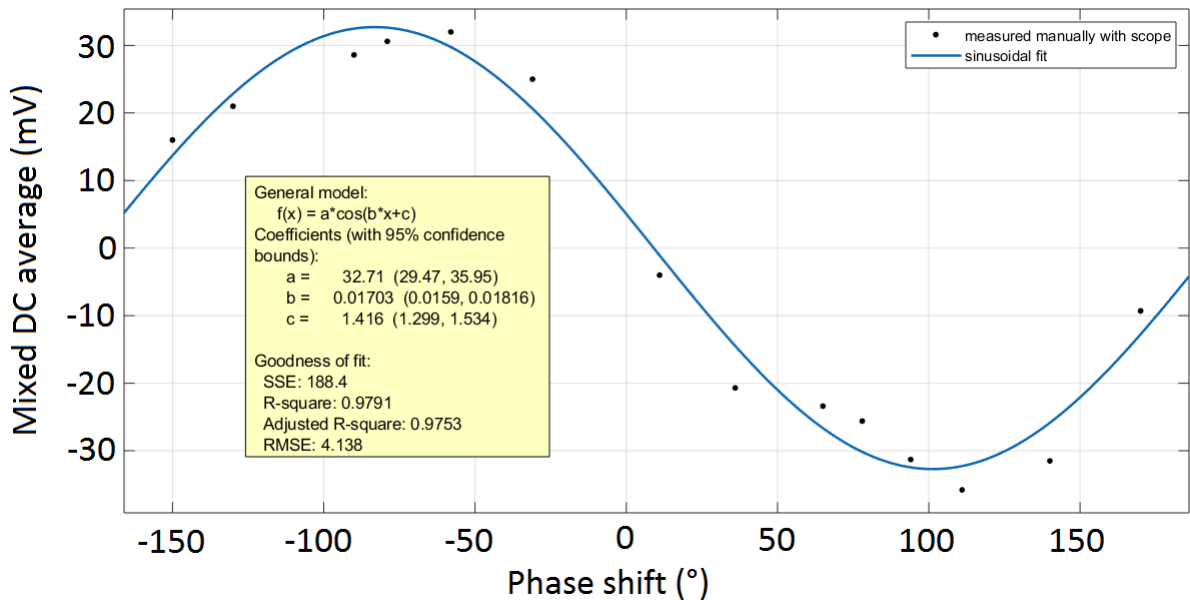


Figure 3.16: Phase noise measurement of the OPLL with fitting data

Fitting the data with a sinusoidal function provides us with the fitting data in figure 3.16. We measured the AC RMS of the mixed signal to be $160\mu\text{V}$, and use that to determine the phase noise to be:

$$\text{PN} = \arcsin\left(\frac{0.16}{32.4}\right) = 0.28 \text{ deg} \quad (3.30)$$

This ranges within the required boundaries. The stable phase relation was also confirmed by observing the two separate signals in the XY-mode of the oscilloscope. The Lissajous figure remained stable in this state, indicating a stable phase relation:

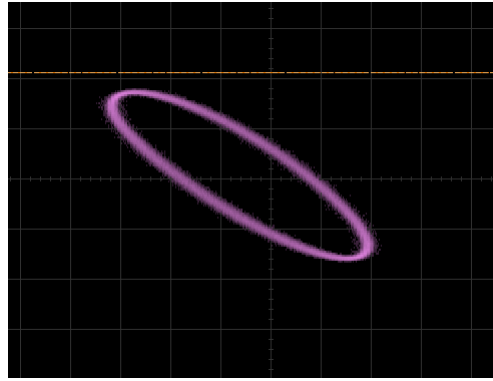


Figure 3.17: X-Y relation of down-mixed beating signal and signal from wavegen

3.4.4 Long-term stability of the lasers

We need to make sure the output of our two lasers remains stable over long time periods. The pulse lengths are only very short, but long term measurements with many steps would be impossible with a high degree of precision if the laser power drifts or is prone to high fluctuations. We took long term measurements of the laser power for both lasers and found them to be sufficiently stable. Over a period of 8min 20s, the standard deviation was $255\mu\text{V}$ with a mean value of 0.998V and a signal to noise ratio of 0.03% for the master laser and $677\mu\text{V}$ with a mean value of 3.276V and a signal to noise ratio of 0.02% for the slave laser.

3.4.5 Power calibration of Raman beams

To calibrate the relation between the voltage sent to the VVA and the laser power at the position of the atoms, we optically measure the power of the two combined Raman laser beams. We measure right behind the vacuum chamber, after both beams have completely passed through it: To obtain the optical power at the position of the atoms from this measurement, we have to factor in the absorption from the two glass plates of the vacuum chamber and the fact that there are two beams. The measured power is therefore corrected in the following way:

$$P_{\text{corr}} = \frac{P_{\text{meas}} * \sqrt{0.84}}{2} \quad (3.31)$$

Plotting the power at the atoms against the voltage we send to the VVA, we can extract a calibration function from figure 3.18. The resulting calibration function is implemented in the control software, and to check if the calculated power at the atoms corresponds to what we program, we measure the light shift at four different Raman powers and compare them to the calculated light shift, see figure 3.19.

The results are in agreement with the theoretical prediction. So we can confidently assume that the power at the position of the atoms is correct as well.

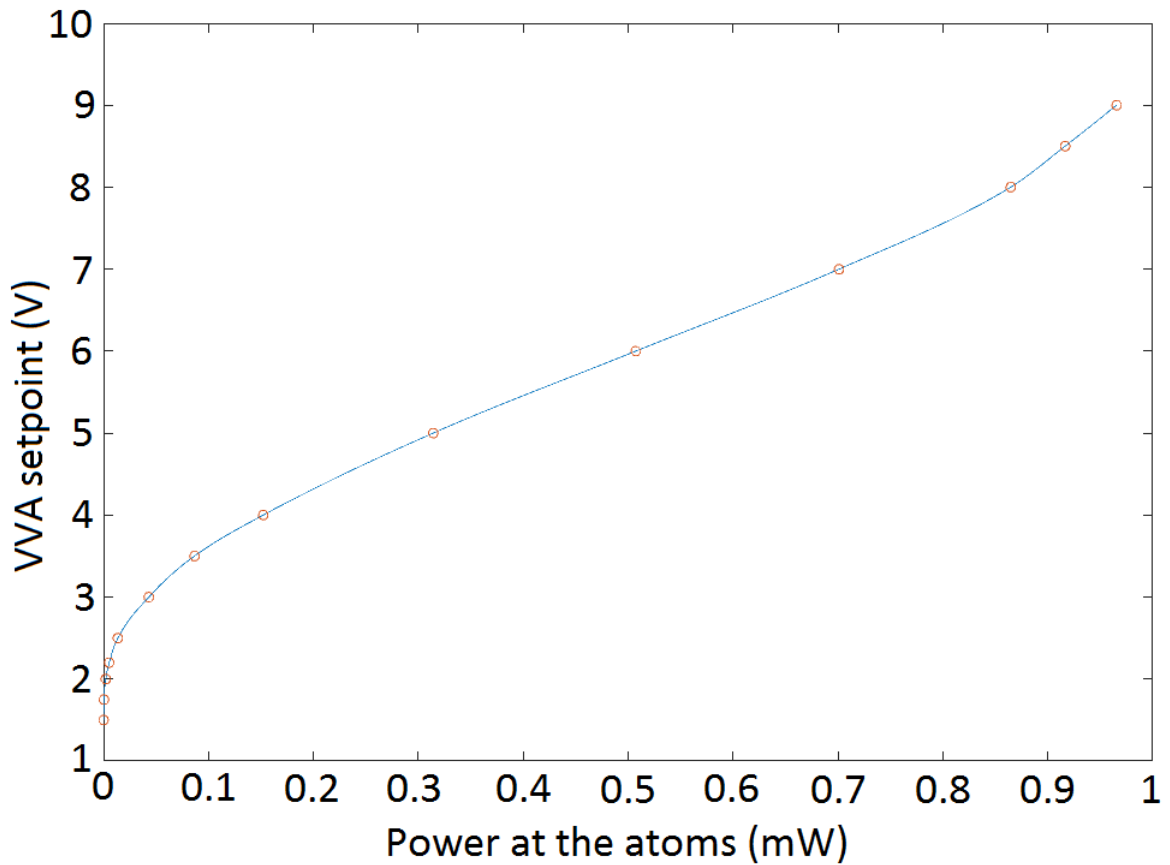


Figure 3.18: Calibration plot for the Raman beams

3.4.6 Time calibration for Raman pulses

In the next step, we check whether the pulse duration we program for the Raman pulses corresponds to the actual length of the pulse as seen by the atoms. We optically measured the pulses using a photo diode and integrated the light intensity to get the effective pulse length. Normalizing that by a maximal-amplitude square pulse and plotting it against the pulse lengths that were programmed gives us figure 3.20.

In orange, we see the line through the origin to compare and clearly see that our data in blue deviates from that. We have to compensate for an offset by changing the programmed pulse length. To find out by how much, we fit the measured light intensity with a linear model $f(x) = a \cdot x$. Points at times $t < 300\text{ns}$ were excluded, see the red crosses in figure 3.21, to achieve a better fitting model. The resulting discrepancies for shorter pulses below 150ns, as seen in the resulting corrected pulse lengths in figure 3.22, are not an issue, since we are limited by our Rabi frequency to $\pi/2$ pulses of around 200ns. After the correction, we see a much better agreement of the observed pulses and the programmed pulses. We use this model to adjust our programmed pulse lengths.

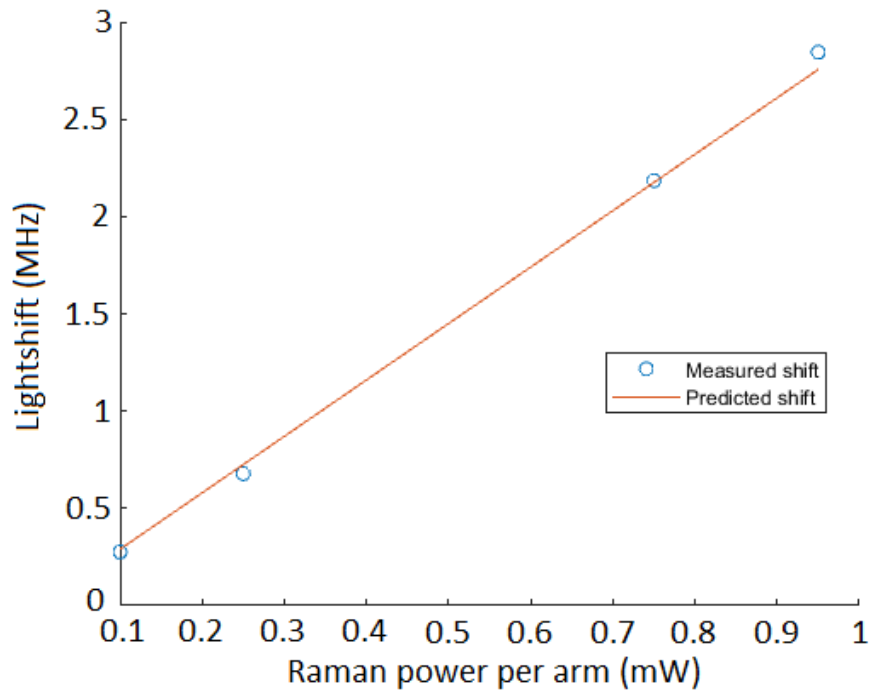


Figure 3.19: Comparison of calculated and measured light shift

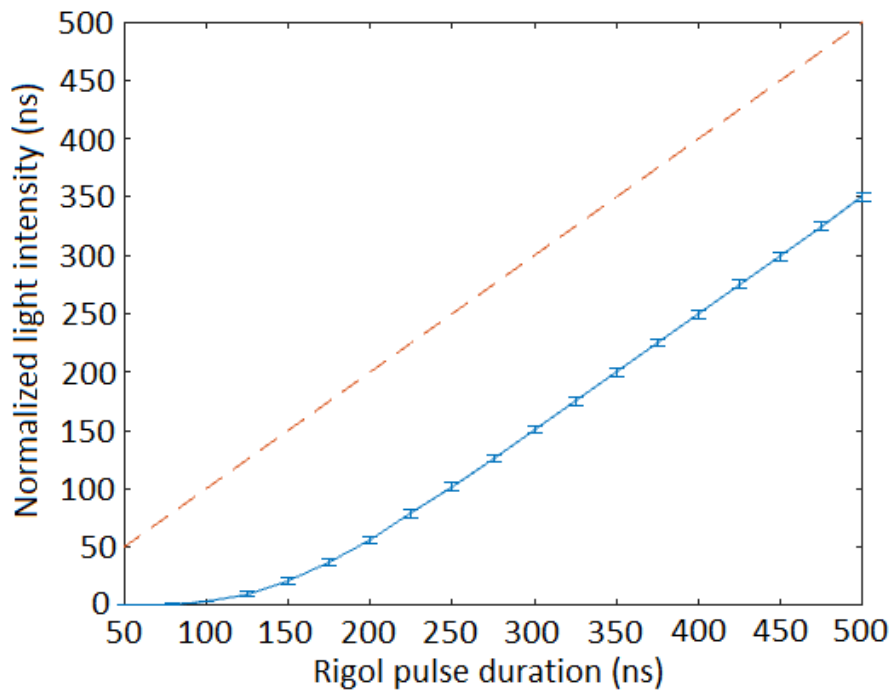


Figure 3.20: Integrated light intensity against programmed pulse length

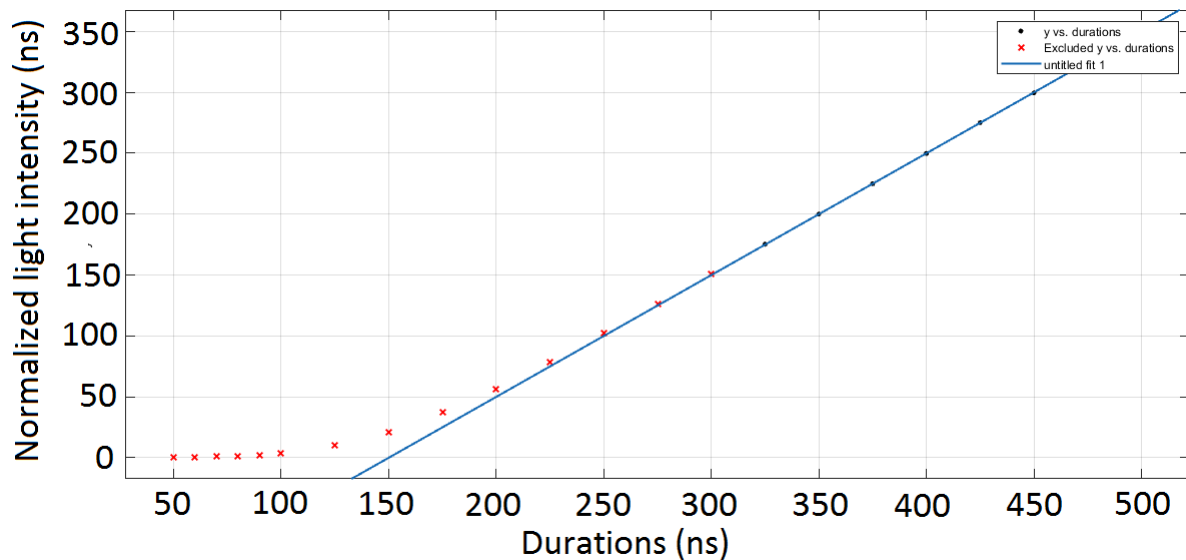


Figure 3.21: Fit for pulse length calibration

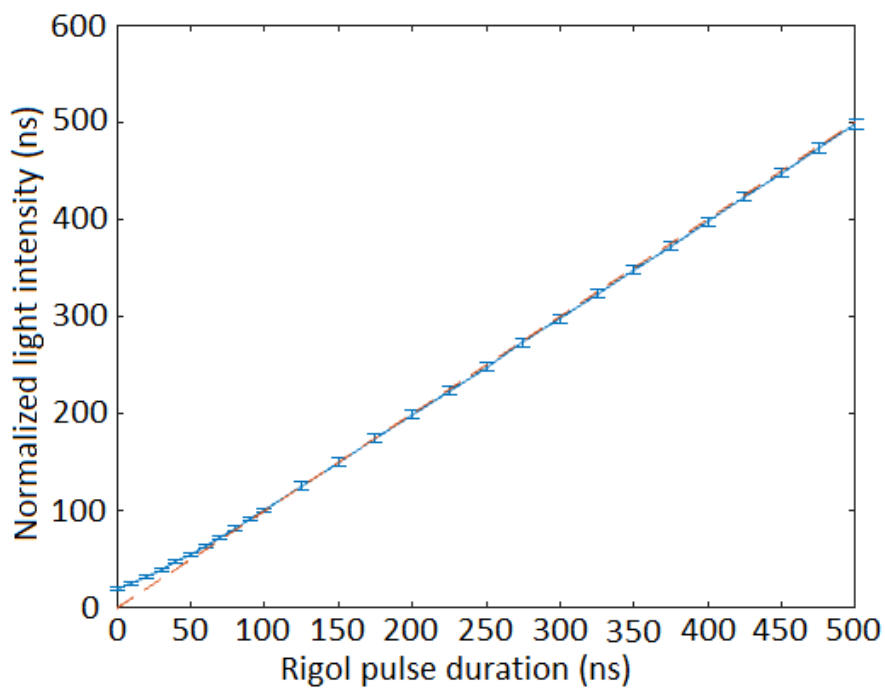


Figure 3.22: Corrected pulse lengths

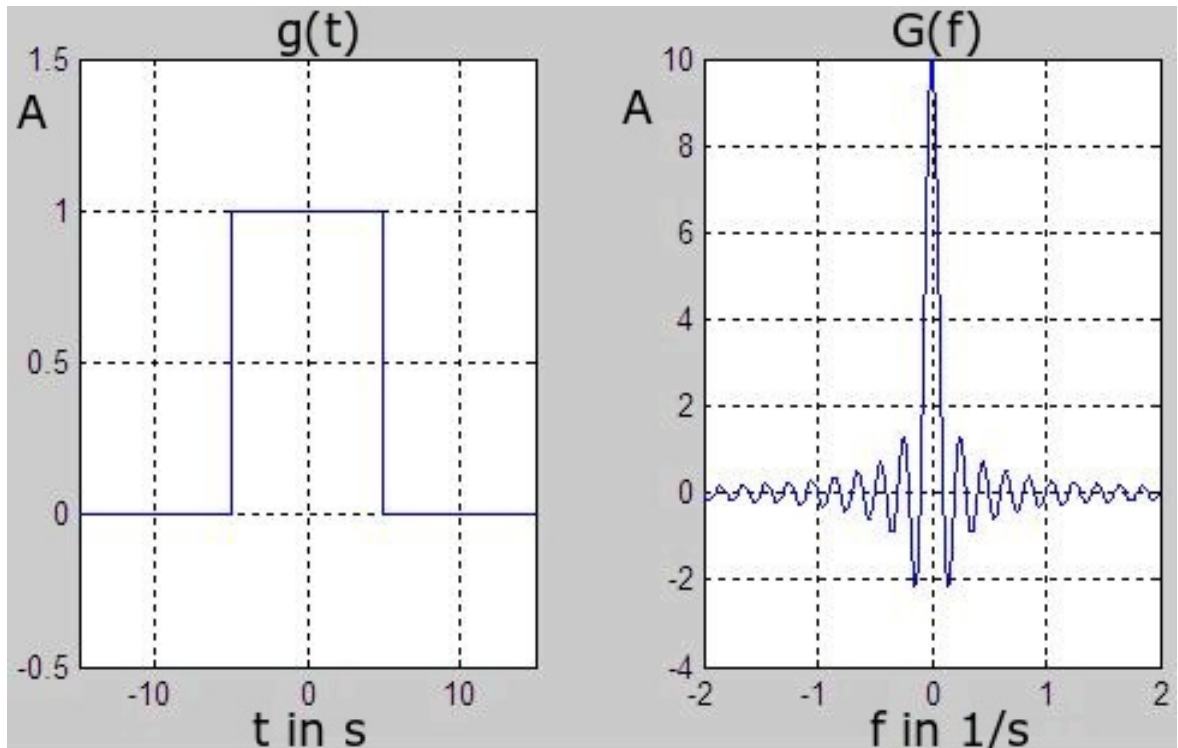
Experimental Procedure

After the setup and calibration of our devices, I will now cover the experimental procedure we employed. I will go over each step individually and present as well as discuss the results.

4.1 Raman spectroscopy

Before we can measure the Rabi frequency, we have to determine the exact transition frequency of the atoms in the lattice. For that, we use a spectroscopic method, which can also be used to determine the spin flip efficiency. Without the Raman beams, this procedure was performed with a spatially broad microwave pulse, which was also the platform for the pulses in other applications. There, the Rabi frequency was limited to around 50kHz, meaning the pulse length for a π -pulse, for example, was limited to $10\mu\text{s}$. The Raman beam setup allows us to reach Rabi frequencies of up to 1.4MHz, which corresponds to π times down to $0.36\mu\text{s}$.

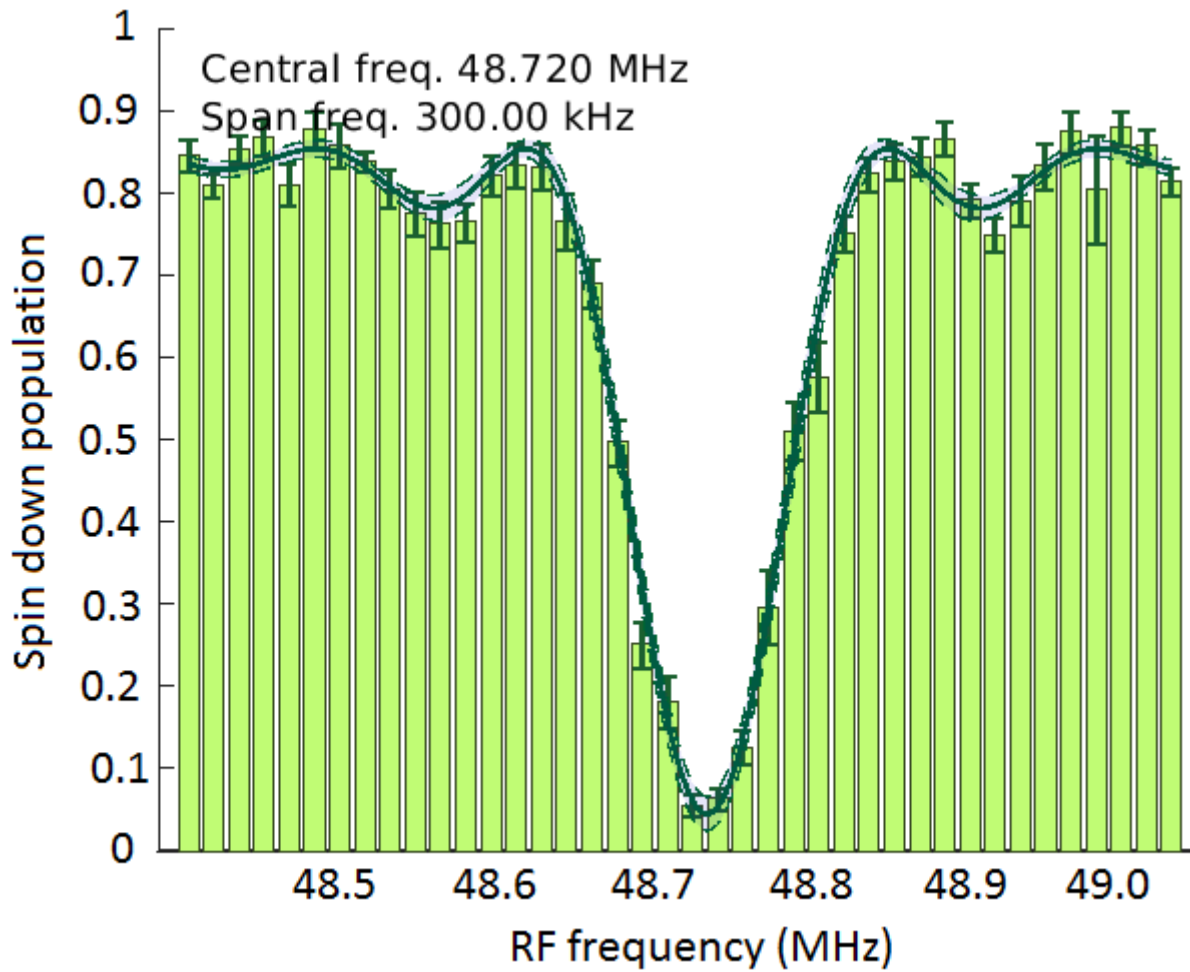
There are two principal types of spectroscopy pulses we employ. A fast rectangular pulse and a spectrally narrow Gaussian one. The rectangular pulse uses the maximally possible Rabi frequency and produces the fastest possible spin flip. The pulse is spectrally broad, which is advantageous in this case: We don't expect the transition frequencies of all atoms to be identical due to variations in the magnetic field both in time and space and to varying light shifts because the atoms are not radially cooled to their vibrational ground state. The disadvantage is that we cannot locally address single atoms with it. Doing that would require spectrally narrowing the pulse by changing the Rabi frequency and the time. Since the Fourier transform of the box function is the sinc function, see figure 4.1, the spectrum of the square pulse would always have these side peaks, which is problematic for locally addressing pulses [14].

Figure 4.1: Box function $g(t)$ and Fourier transform $G(f)$ [34]

The Gaussian shaped pulse is then used for a better spectral resolution. Also, it shields the qubit from decoherence due to dephasing. The reason is that the qubit is most sensitive to dephasing decoherence in an equal superposition state, while there is no sensitivity in the pure states. With the Gaussian π -pulses, for example, the qubit will spend less time in that superposition state. So for a similar spectral resolution, due to the reduced dephasing, the transfer efficiencies of the Gaussian pulses are higher.

The spectra are recorded according to the following procedure. We load the atoms into the lattice and measure the initial number through fluorescence imaging. We lower the lattice and initialize the atoms in the $|\uparrow\rangle$ state through optical pumping, as explained in chapter 2.1.4. Then the atoms are exposed to the chosen microwave pulse whose frequency changes in each iteration over a specified span. That way, we scan the transition frequency step by step and use the push-out technique after each iteration. Here, the atoms are projected into either the $|\uparrow\rangle$ or the $|\downarrow\rangle$ state and the atoms in the $|\uparrow\rangle$ state are removed from the lattice. We again measure the population in the $|\downarrow\rangle$ state using fluorescence imaging. This procedure is repeated until we get a spectrum with sufficient statistics.

Measuring these spectra with Raman beams instead of the microwave is not principally different. The frequency steps are now achieved by changing the reference signal of the OPLL. Several spectra were taken. For the spectrum in figure 4.2, the power of the Raman beams was adjusted so that the Rabi frequency matches that of the microwave used in earlier experiments. We used a square pulse of $8.2\mu\text{s}$ length and a total power of around $50\mu\text{W}$ per beam.

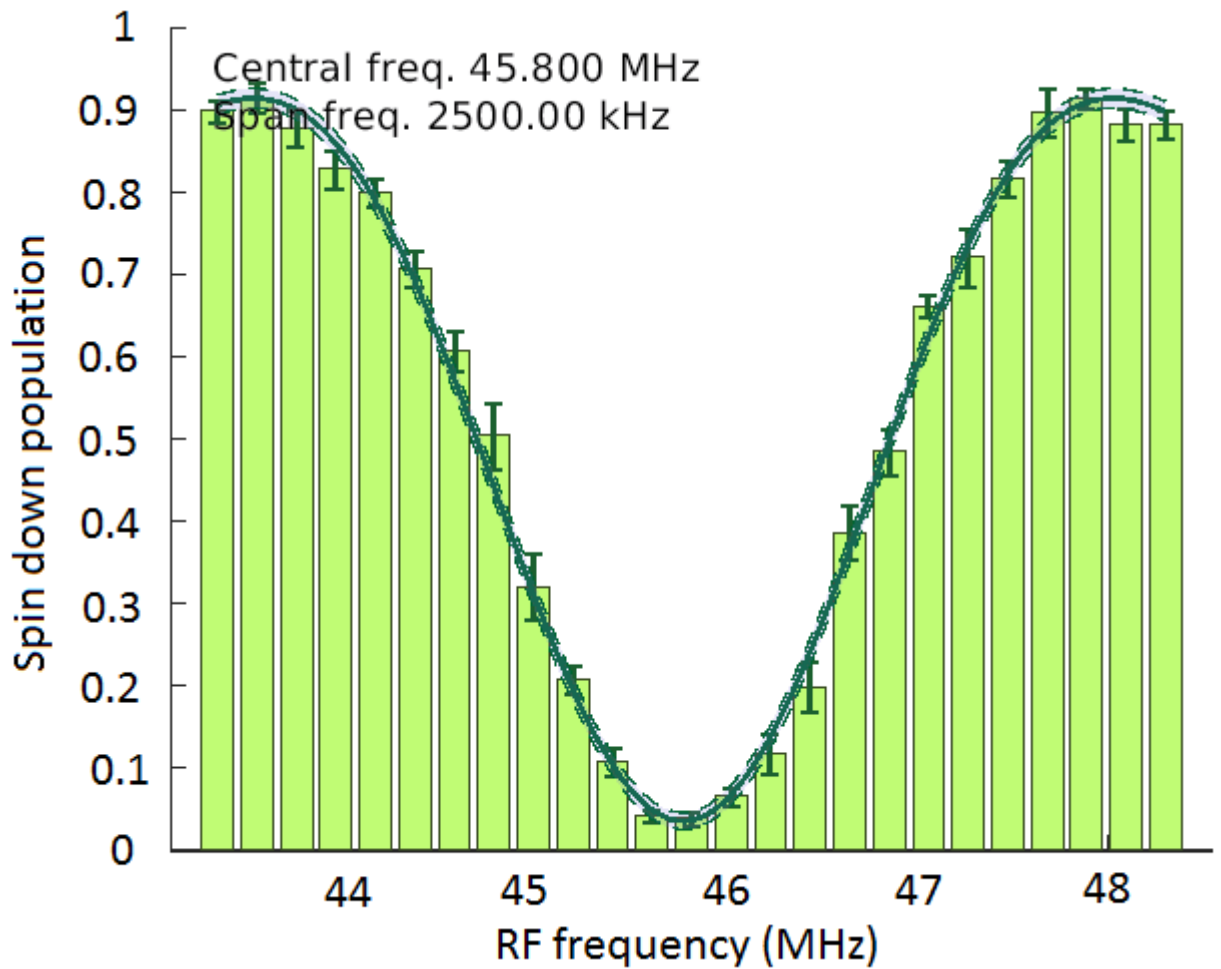


$1 - \alpha$	95.0%
Reduced χ^2	1.460
Baseline	0.853 ± 0.005
Rabi frequency[kHz]	52.012 ± 4.249
Frequency offset[MHz]	48.736 ± 0.001
Pulse duration[μs]	8.2
Raman transfer efficiency	1.0 ± 0.05

Figure 4.2: Raman spectrum with $8.2\mu\text{s}$ pulse length and $50\mu\text{W}$ of power per beam

The picture is similar to what would have been observed with a microwave pulse. The Rabi frequency is calculated after fitting the data to be around 52kHz. This confirms that the process works as expected, a microwave pulse of that length yielded a Rabi frequency of around 56kHz.

As a next step, we increased the power of the Raman beams as high as possible at the position of the atoms, 1.19mW per beam. The pulse was now also substantially shorter at 375ns and thus spectrally broader, see figure 4.3.



$1 - \alpha$	95.9%
Reduced χ^2	1.299
Baseline	0.913 ± 0.006
Rabi frequency[kHz]	1404.0
Frequency offset[MHz]	45.756 ± 0.011
Pulse duration[μ s]	0.375
Raman transfer efficiency	0.967 ± 0.005

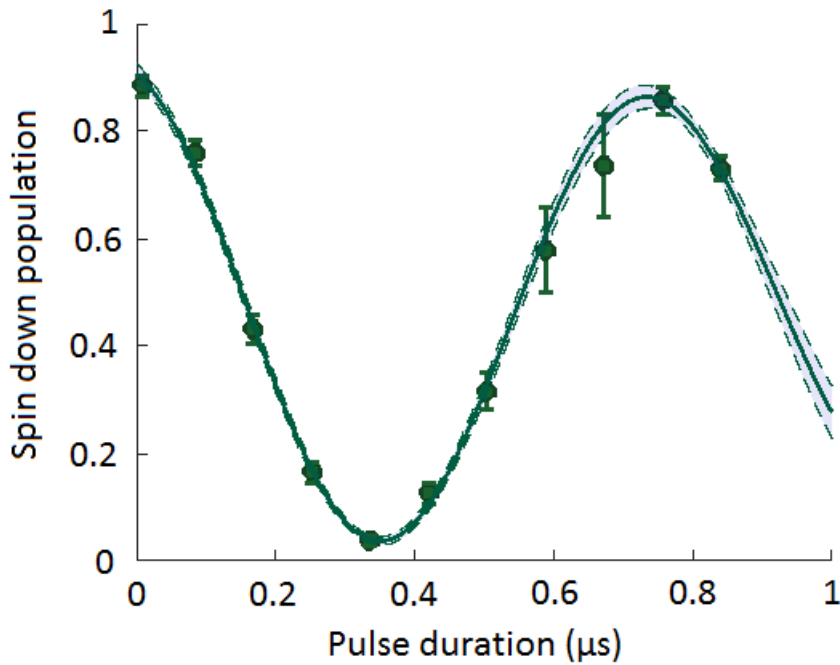
Figure 4.3: Raman spectrum with 375ns pulse length and 1.19mW of power per beam

As expected, the spectrum is substantially broader, more than one order of magnitude, which is a consequence of the shorter duration. We again fit the data and extract a central frequency of 45.8MHz. This is then set as the reference frequency of the OPLL for the following experiments. The Rabi frequency is 1.404MHz, though in this fit, this was set as a fixed parameter since it could be calculated more precisely from the Rabi oscillation measurement explained in the next section.

4.2 Rabi oscillation measurement

To measure the Rabi frequency at the transition frequency of 45.8MHz, we can now adjust the pulse lengths t . With the different pulse lengths, following equation 2.20, we change the population state w of the atoms. Given that under continuous exposure to the resonant Raman light, the atom sample performs Rabi oscillations, it is clear that by performing discrete steps, we can trace the oscillation and extract the Rabi frequency using a sinusoidal fit.

For the maximum power we could achieve with the Raman beams, 1.19mW per beam, we plot the measured oscillation in figure 4.4.



$1 - \alpha$	68.0%
Reduced χ^2	0.863
Survival	0.907 ± 0.035
Rabi frequency[MHz]	1404.0 ± 0.019
Rabi phase[rad]	0.296 ± 0.074
Offset[μ s]	0.020 ± 0.012
Radial temperature[μ K]	7.243 ± 2.439
Trap depth[μ K]	80

Figure 4.4: Rabi oscillation for Raman beams at 1.19mW

Fitting a sinusoidal function gives us the fitting parameters in the table in figure 4.4. The Rabi

frequency is at $1.404 \pm 0.019\text{MHz}$. This is around 100kHz off the theoretical value we calculated in 3.4.1. We can calculate the $\pi/2$ time as $t_{\pi/2} = 187.5\text{ns}$. The plot also shows that the oscillation does not start at a relative population of 1 but rather a little below that. This is a result of our survival, the fraction of atoms staying trapped through the entire process, which was not at 100% , meaning we lose atoms due to for example off-resonant scattering with lattice photons. Another factor was the state preparation, which included a microwave-transfer into the lower qubit state, which is not 100% efficient either.

Generally speaking, Rabi oscillations are not very sensitive to dephasing. This is because they make use of an effect called dynamic decoupling, see [35] and [36]. This can be seen prominently in this plot from [14], see figure 4.5.

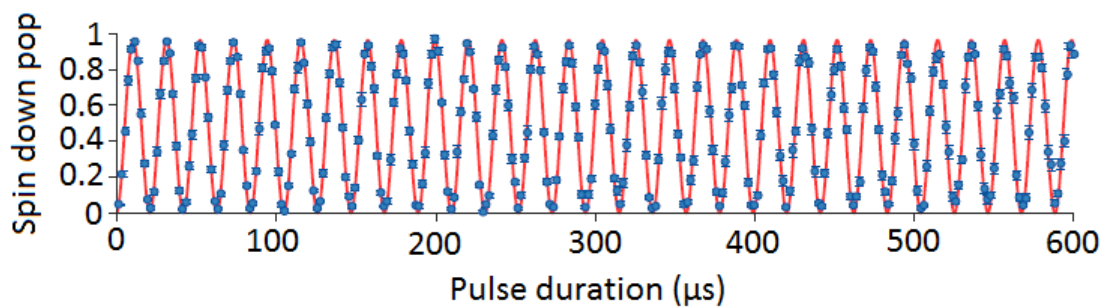


Figure 4.5: Microwave induced Rabi oscillations with $\Omega_R = 48\text{kHz}$

Here, the same process as described above is used to measure the Rabi oscillations induced by Microwave radiation. The purpose of this measurement was to determine the $\pi/2$ time, which is extracted from this plot as $4.82\mu\text{s}$. It can be seen clearly that even after 30 oscillations between the $|\uparrow\rangle$ and $|\downarrow\rangle$ states, and pulse lengths of up to $600\mu\text{s}$, the contrast does not noticeably decay.

In contrast, see a measurement with the Raman lasers in figure 4.6, which was continued up to pulse lengths of $15\mu\text{s}$.

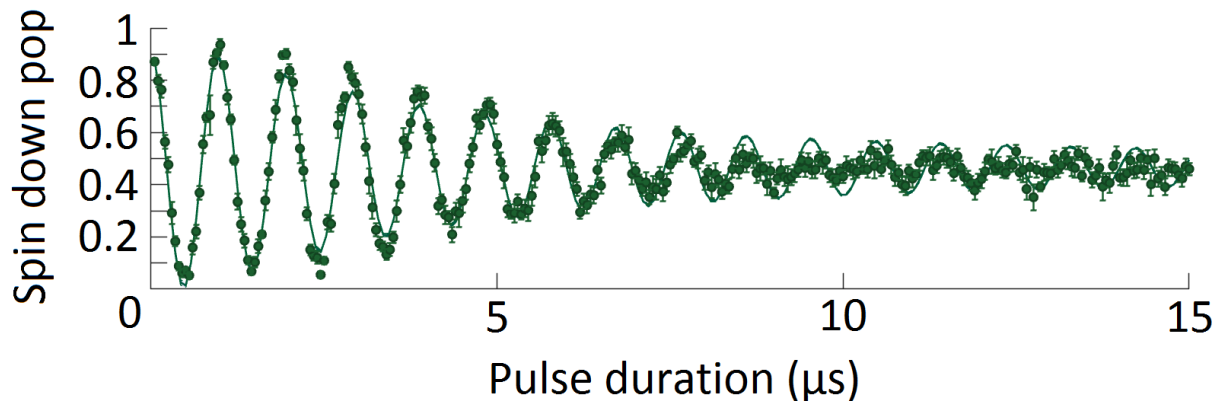


Figure 4.6: Rabi Oscillations induced by Raman beams at 1.1mW per beam

$1 - \alpha$	68.0%
Reduced χ^2	3.844
Survival	0.935 ± 0.020
Rabi frequency[MHz]	1068.0 ± 0.001
Rabi phase[rad]	0.158 ± 0.030
Offset[μ s]	-0.003 ± 0.010
Radial temperature[μ K]	5.094 ± 0.237
Trap depth[μ K]	80

From the data, we determined the Rabi frequency to be 1.068MHz, but it is also obvious how quickly the contrast between the $|\uparrow\rangle$ and $|\downarrow\rangle$ states decays. What we see here is a dephasing effect, which is new to the system due to the introduction of the Raman beams, and which did not occur in the earlier experiments with the microwave pulses.

The microwave pulses are applied broadly, covering the entire volume of the vacuum chamber which houses the optical lattice. As such, there were no spatial inhomogeneities that the atoms would experience. The Raman beams, however, since they are overlapped with, and traverse the same focusing optics as the lattice beams, are focused to a beam waist of $17\mu\text{m}$ at the position of the atoms. Their intensity profile is Gaussian, meaning the atoms experience a lower intensity at the edges of the beam than along the optical axis.

Following the general expression for the Rabi frequency:

$$\Omega_{i,j} = \frac{\vec{d}_{i,j} \vec{E}_0}{\hbar} \quad (4.1)$$

We see that the Rabi frequency directly depends on the intensity of our Raman beams, meaning Rabi frequencies differ depending on the position of the atoms. So for a given pulse length with the different Rabi frequencies affecting the atoms, a different Rabi phase is applied. For example, if we program a π -pulse, the atoms in the center of the beam will change state entirely due to the full π -pulse, while the atoms situated at the outer edges of the beam might only experience a fraction of a π -pulse and not get transferred completely. During the subsequent push-out after the pulse, these atoms are not removed and the measured population is higher than it should be.

In pulses with greater pulse durations, where the difference in Rabi phase is allowed to accumulate longer, this effect is stronger and the measured population is higher yet. This perceived decay of the Rabi oscillation is a measure of how far the atoms are spread apart radially, effectively a measure of how high the radial temperature is. The faster the oscillation decays, the more spread out the atoms and the higher the radial temperature.

4.3 Raman thermometry

In principle, measuring the decay of the Rabi oscillation, we can determine the radial temperature of the atom sample. We tested that by repeating the measurement for the Rabi oscillation at different powers of the Raman beams and fitting it with a model to extract the radial temperature. In case the power of the Raman beams were subject to a drift in time over the duration of our experiment, we did not perform the measurements for the different laser powers sequentially from 0 – 1mW. Instead,

we scattered the measurement points for the different powers randomly in multiples of 0.1mW and avoided the systematic error that would have resulted from a drift.

There are a number of decoherence effects affecting our atoms, see e.g. [9] or [14], which lead to a faster apparent decay of the Rabi oscillation. If the laser power is low and the corresponding Rabi frequency as well, these effects are dominant. This is because at low Rabi frequencies, where the population changes state quite slowly, effects with a similar time constant are more prominent. The model we use to extract the radial temperature from the decay of the Rabi oscillation interprets the influence of these decoherence effects as a higher radial temperature, since a higher radial temperature would also lead to a faster decay. At higher powers and Rabi frequencies, these effects are not as pronounced and the decoherence due to the Gaussian intensity profile mentioned earlier is the primary effect influencing the speed of the decay. This distinction is critical as we interpret figures 4.7 and 4.8. In figure 4.7, the laser power per beam is plotted against the Rabi frequency to confirm the Rabi frequency rises with the inducing laser power, as expected from equation 4.1. Indeed, the Rabi frequency rises linearly with the laser power. The visible discrepancy to the calculated frequencies is a result of the differing Rabi frequencies within the atom sample.

In figure 4.8, we see the radial temperature depending on the laser power. We see clearly that the highest temperatures are measured for the low laser powers while it seemingly drops as the power rises. It converges to around $4.2\mu\text{K}$ at 0.9mW. This drop is caused by the other decoherence effects subsiding, and we clearly see them becoming less pronounced with rising laser power. At the high laser powers we measure the actual radial temperature. Unfortunately, we were limited by how much power we could bring to the atoms with the Raman beams. It would be interesting to expand the measurement parameters and get better statistics. The last plot in figure 4.9 shows the measurement points plotted against their measurement number, just to confirm that there are no systematic effects at play.

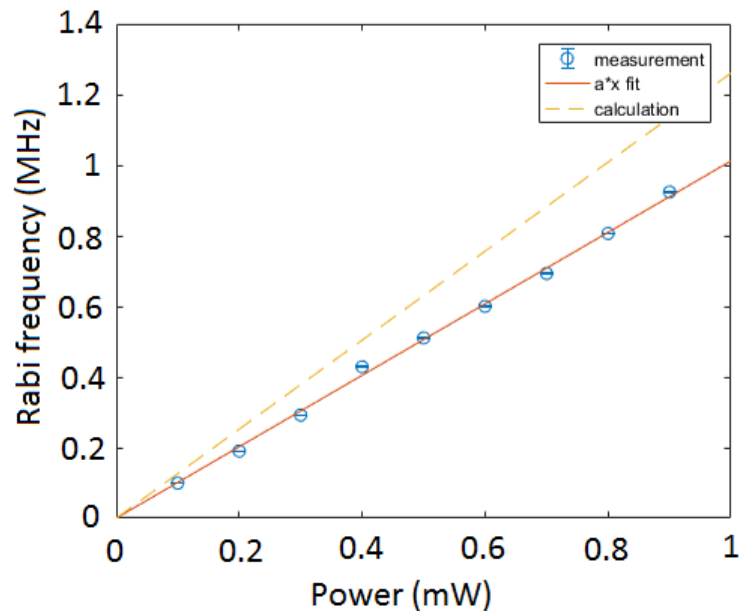


Figure 4.7: Rabi Frequency depending on the laser power

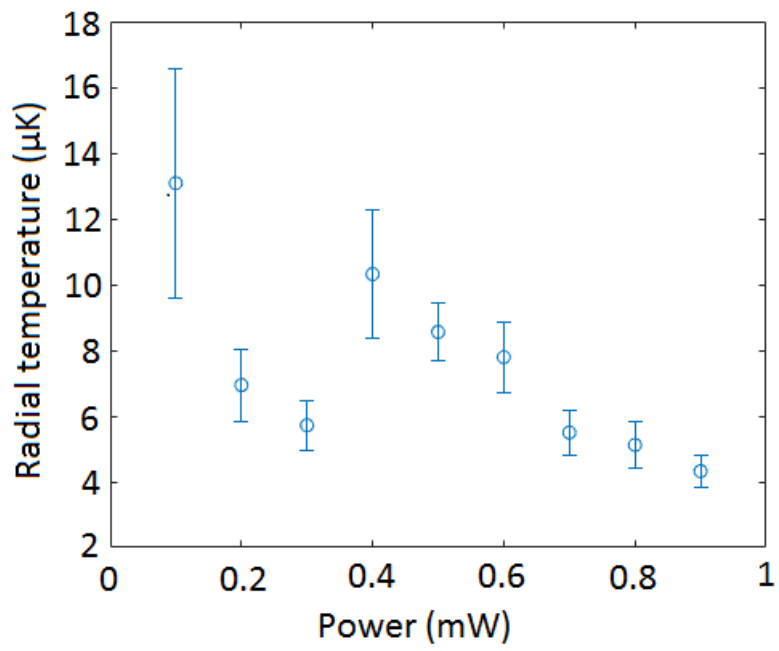


Figure 4.8: Radial temperature against laser power

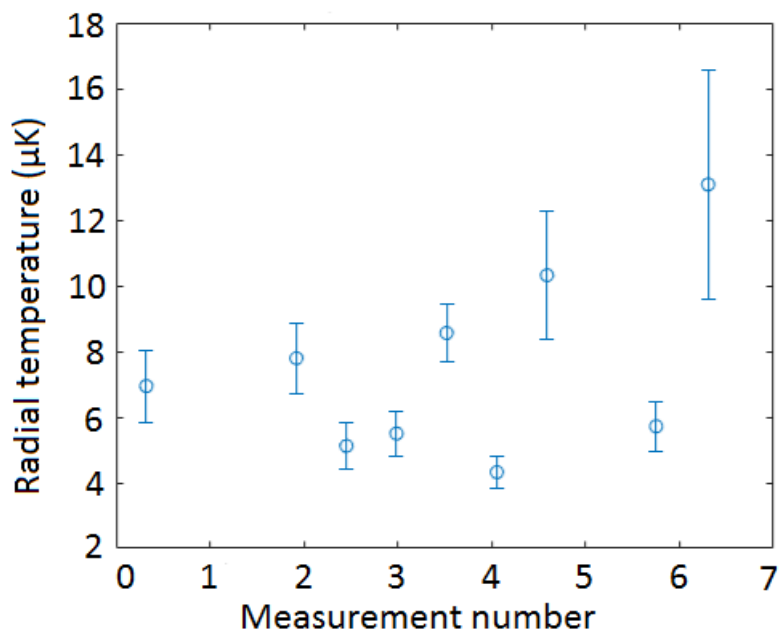


Figure 4.9: Radial temperature against measurement number

4.4 Ramsey interferometry

4.4.1 Measurement scheme for quantum speed limit

To measure the quantum speed limit using Ramsey interferometry, we will proceed similarly to the method described in section 2.3. The step by step procedure can be seen in figure 4.10. It starts with the atom prepared in the ground state, which is then transferred into a superposition state $|\psi_i\rangle$ by a $\pi/2$ -pulse:

$$\psi_i = \frac{1}{\sqrt{2}}(|\uparrow, n=0\rangle - |\downarrow, n=0\rangle) \quad (4.2)$$

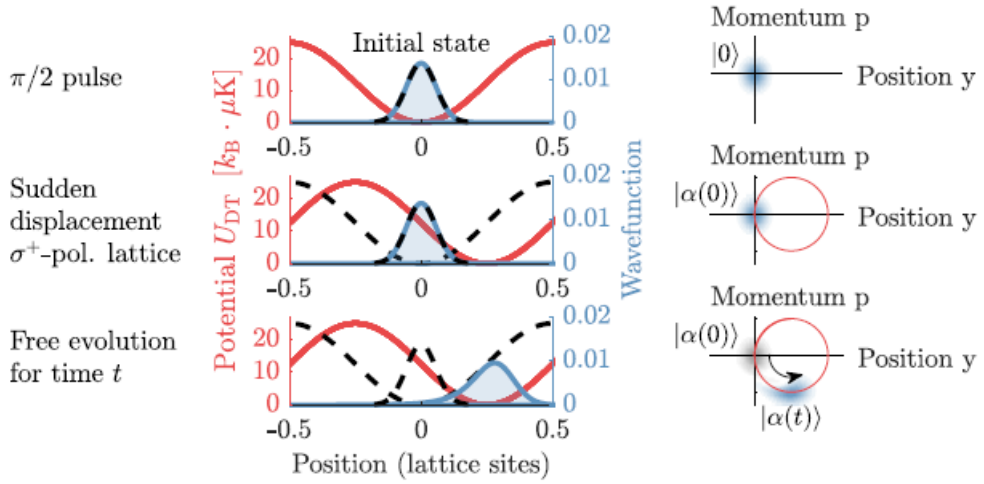


Figure 4.10: Ramsey interferometry measurement scheme for verification of quantum speed limit. The left side shows the step by step measurement scheme, where the red and the blue trace are the lattice potential and wave function position of the $|\uparrow\rangle$ state. The dotted black trace shows the initial position of the potential and the wave function of the $|\downarrow\rangle$ state. The right side corresponds to the same steps in the sequence but shows the wave function in momentum-position space. [37]

Now the σ_+ -polarized lattice is displaced in lattice direction by an amount Δy . We describe this with the displacement operator $D(\alpha) = \exp(\alpha \hat{a}^\dagger - \alpha \hat{a})$. For the free evolution time t , the wave packet in the $|\uparrow\rangle$ state is now in the shifted position, while the wave packet in the $|\downarrow\rangle$ state remains in the σ_- -lattice and the original position and serves as the reference wave function. The coherent atom state in the shifted lattice is described by $|\alpha(t)\rangle$:

$$|\alpha(t)\rangle = e^{i\omega t} D(\alpha)|0\rangle = e^{i\omega t} e^{-|\alpha|^2/2} \sum_n = 0^{\text{inf}} \frac{\alpha^n}{\sqrt{n!}} |n\rangle \quad (4.3)$$

After the time Δt , the Ramsey time, the second $\pi/2$ -pulse is applied and the wave function is described by the superposition state:

$$|\psi(t)\rangle = \frac{1}{2} |\uparrow\rangle \otimes [|\alpha(t)\rangle - D(\alpha)|0\rangle] - \frac{1}{2} |\downarrow\rangle \otimes [D(-\alpha)|\alpha(t)\rangle + |0\rangle] \quad (4.4)$$

After that, the atoms are projected onto the $|\downarrow\rangle$ state using the push-out technique and a survival meas-

urement. By varying the phase difference of the second pulse to the first pulse, we can trace the Ramsey fringe and determine the overlap of initial ground state and final state at time t by extracting the contrast:

$$|\langle \downarrow | \psi(t) \rangle|^2 = \frac{1}{4} |\langle \alpha(t) \rangle + D(\alpha) | 0 \rangle|^2 \quad (4.5)$$

$$= \frac{1}{2} + \frac{1}{2} \Re[\langle \alpha(t) | D(\alpha) | 0 \rangle] \quad (4.6)$$

$$= \frac{1}{2} + \frac{1}{2} \Re[\langle \alpha(t) | \alpha(0) \rangle] \quad (4.7)$$

Figure 4.11 shows a numerical calculation of the overlap and a comparison with the Mandelstam-Tamm and Margolus-Levitin speed limits for different trap depths and lattice shifts [37]. The speed limit in our experiment is given by the Mandelstam-Tamm bound, as it is the larger of the two, the green line in the picture. We also expect a revival of the wave function, the bright line in the top right corner, which is when the wave function overlaps again with the reference wave function after one oscillation period. Factors that influence the revival time, to make it differ from the harmonic period, include the radial distribution of the atoms and the fact that the lattice shift is not infinitely fast. The Margolus-Levitin limit is represented by the red trace. The fidelity as a measure of the overlap between the initial and final states is color-coded, 100% meaning a complete overlap.

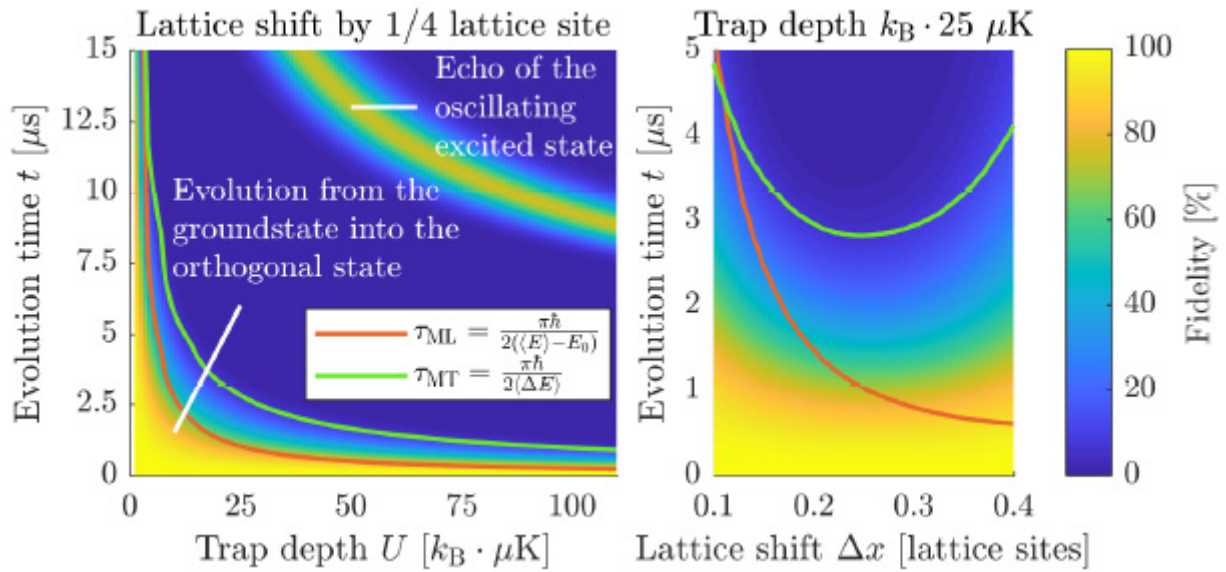


Figure 4.11: Theoretical prediction of quantum speed limit [37]

4.4.2 Phase modulation

Performing Ramsey interferometry with the earlier microwave pulse setup involved the use of an RF generator, which was mixed with a PLDRO and produced phase modulated pulses. To implement the

phase steps for the Raman beams, we had to use a different method, since the pulses are not provided by a separate generator. The Raman beams are phase locked to a reference frequency from a local oscillator, see figure 3.8, we can phase modulate that signal to affect the desired change. The phase modulated signal is connected to one of the inputs of the PFD of the lock, the other input being the mixed down beating signal of the lasers. The lock will now match the phase of the two signals via the fast feedback. Because the PLDRO we use for down-mixing is not phase modulated itself, the phase of the modulated signal will be the same as that of the mixed down one, and in turn also the same as that of the beating signal.

For each different set phase, the lock will transfer that phase to the beating signal of the Raman beams, and we can scan it step by step, as we did in the earlier case with the microwave generator. The tool for phase modulation is a Keysight M3300A FPGA and Digitizer module. Together with the connection module M9022A, it is set into a M9010 chassis, which connects to the computer through a PCIe cable also supplied from Keysight. Finally, the M9048B PCIe Host Adapter supplies the connection to the computer's mainboard. To operate the FPGA from the PC, we use a custom made Matlab class, which allows individual control of the four output channels. Frequency, amplitude and phase can be independently controlled for each of the channels. This setup will now be the "wavegen" in figure 3.8. One of the output channels of the FPGA is programmed to provide the reference signal with the transition frequency found in the spectroscopy measurement and with phase jumps of a defined amplitude and length. At the beginning, the phase will be set to 0. After a defined waiting time Δt_d , see figure 4.12, which has to be long enough that the first $\pi/2$ pulse of the Ramsey sequence can be applied, the phase is then very quickly ramped to the target value, from $0 - 2\pi$. The waiting time also has to include an instrument caused delay, whose length was measured optically. The phase stays at the specified value for the pulse duration. This time has to be longer than the Ramsey time itself to make sure that the second $\pi/2$ pulse is at the target phase. After that, the phase is returned to 0, the initial value. The timing, as seen in figure 4.12, has to be very precise here, so that only the second $\pi/2$ pulse is phase modulated. If both pulses were affected, they would be in phase and the entire atom sample would simply be transferred completely into the lower state. The same happens if none of the pulses get phase modulated.

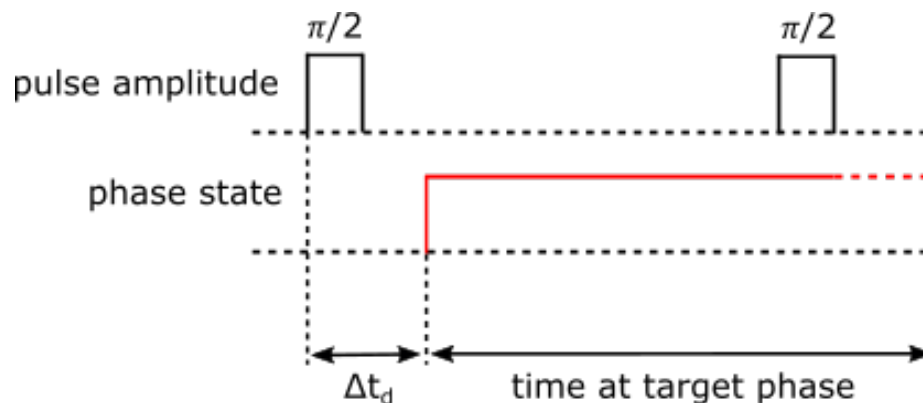


Figure 4.12: Phase jump timing of the Ramsey sequence

This entire process is programmed in a so-called sequence, which defines the shape and timing of the waveforms as the output for one or more of the channels in addition to its previous mode of operation.

Since we only change the phase in the sequences, we will get a phase modulated signal of a frequency and amplitude that was set beforehand. Once the sequences are loaded to the device, we start the execution, and only then will the FPGA wait for a trigger to start the sequence. This allows us to avoid timing issues with the operating speed of the FPGA, the PC, or any other involved electronics. The trigger will then be the same as for the AOM, which, including some time delay adjustments we make to the sequence itself, allows a parallel execution.

4.4.3 Fast Ramsey fringes

We performed Ramsey interferometry in the manner detailed in chapter 2.3. With a Rabi frequency of 1.333MHz, a Ramsey time of 200ns and a $\pi/2$ -pulse time of 187.4ns, we got the data in figure 4.13. The measurement yields the expected results and shows that we are able to reliably perform Ramsey interferometry at these high Rabi frequencies. We observe that the relative population does not reach the maximum or the minimum of either 0 or 1. This is an effect of the decoherence due to the Raman beams. At these high Rabi frequencies, we are able to do the experiments to verify the Mandelstam-Tamm quantum speed limit.

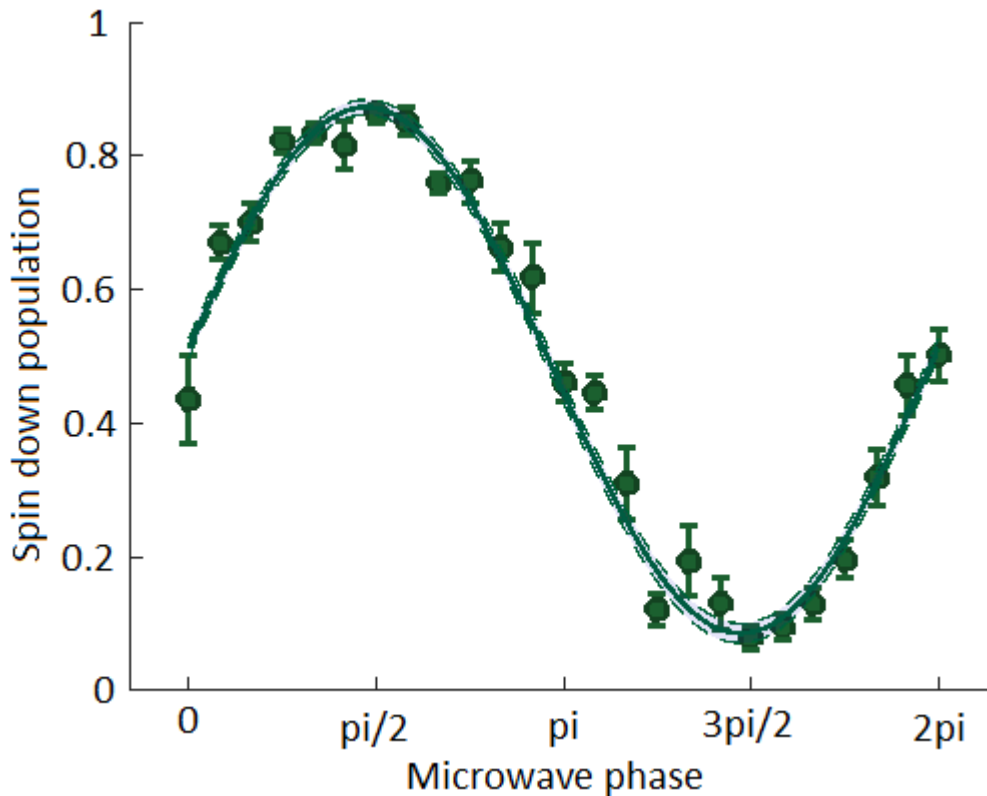


Figure 4.13: Ramsey fringe at 1.333MHz Rabi frequency

4.4.4 Quantum speed limit measurements

Before we can measure the fringes for the verification of the quantum speed limit, we have to address some timing issues. As mentioned above, there is a delay, measured to be around 690ns, between the trigger, ordered by the PC, and the actual pulse. It is incorporated into the execution sequence as part of the delay time Δt_1 , see figure 4.14. This delay will be the combined unavoidable hardware delay and the necessary waiting time for the first $\pi/2$ pulse to occur, before the lattice shift between the two pulses can begin.

The lattice shift itself is problematic, as ideally, it would be instantaneous, in order to be able to scan the Ramsey time starting from 0. In reality, the transport ramp takes about $2.34\mu\text{s}$ for a shift of 1/4 of a lattice site, which has to be taken into account. In figure 4.14, we see the timing scheme for the lattice shift. The red curve represents the transport, with the transport ramp on the left side after the first $\pi/2$ -pulse. The lower state represents the initial position of the lattice, the upper state the final position. The lattice then stays in the second position for the second pulse and is reset before the next measurement. The shift will occur with the σ_+ -polarized lattice, while the σ_- -polarized lattice stays in place as the reference.

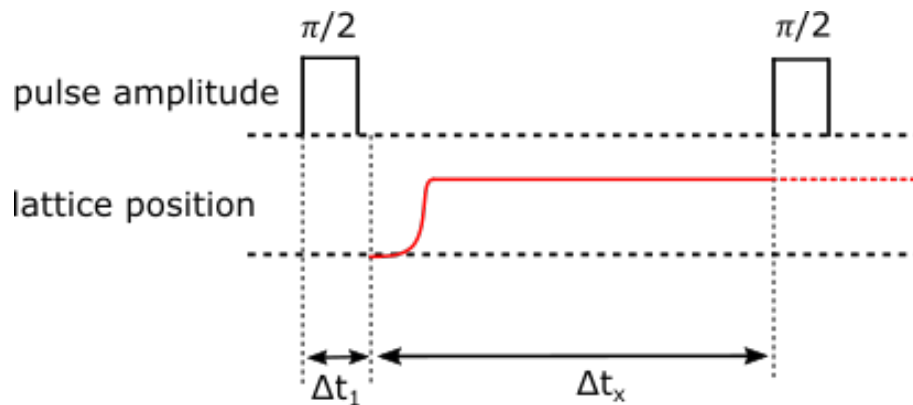


Figure 4.14: Pulse timing for MST measurement

To confirm that we are performing the pulse and lattice shift sequence as planned, we shift the lattice by 1/4 of a lattice site and optically measure the lattice shift including the two $\pi/2$ pulses in figure 4.15. The upper picture shows only the transport ramp itself, while the lower picture shows the transport ramp with a length of $2.34\mu\text{s}$ and the two pulses at either end. The measured pulse timing agrees with our planned sequence in figure 4.14 quite well. Δt_x from the schematic picture in figure 4.14 can be found again between the two dotted vertical lines.



Figure 4.15: left: lattice shift; right: lattice shift with 2 Raman pulses

Similar to the way we extract the T2 time in chapter 2.3, we need to measure several Ramsey fringes. We vary the Ramsey time and extract the contrast for each fringe. Including the delays discussed above, when we program a certain time in the PC, it will correspond to Δt_x , from the start of the transport ramp until the beginning of the second $\pi/2$ pulse. After the second pulse, the population in the $|\downarrow\rangle$ state is measured and the next pulse iteration is applied.

Each extracted contrast for a given Ramsey time will be paired with a reference value, where we do not shift the lattice at all, but which is measured with the same Ramsey time. That gives us a way to normalize our measurement, since we only want to measure the population change due to the transport and exclude other decoherence effects. We perform several measurements at different trap depths, see the table below.

Beam power [mW]	Trap depth [μK]
0.5	14.286 ± 0.372
1	28.689 ± 0.198
2	57.813 ± 0.435

In each measurement, the Ramsey time is scanned from $2\mu\text{s}$ to $40\mu\text{s}$ in $1\mu\text{s}$ steps, though in some cases, the first points were taken in $0.5\mu\text{s}$ intervals.

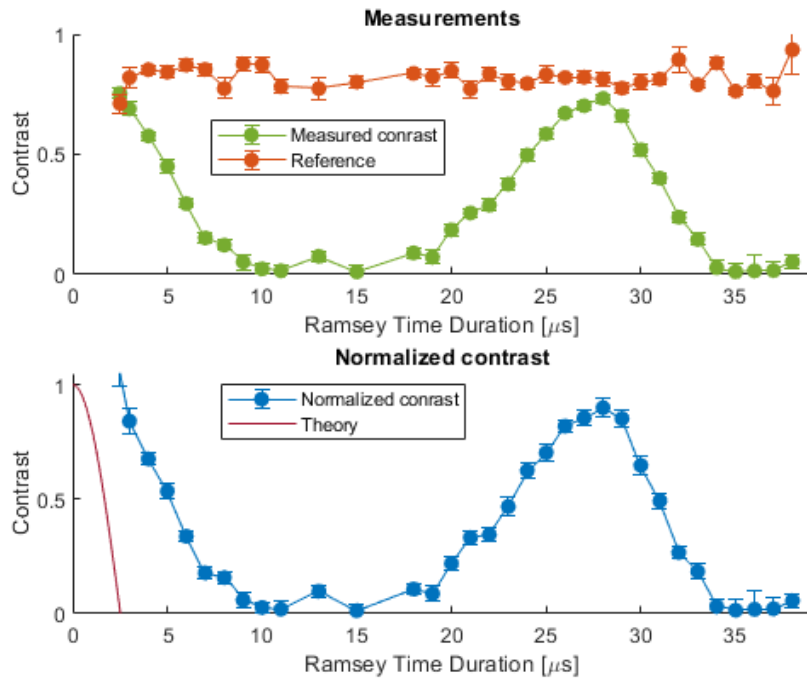


Figure 4.16: Quantum speed limit measurement at 0.5mW

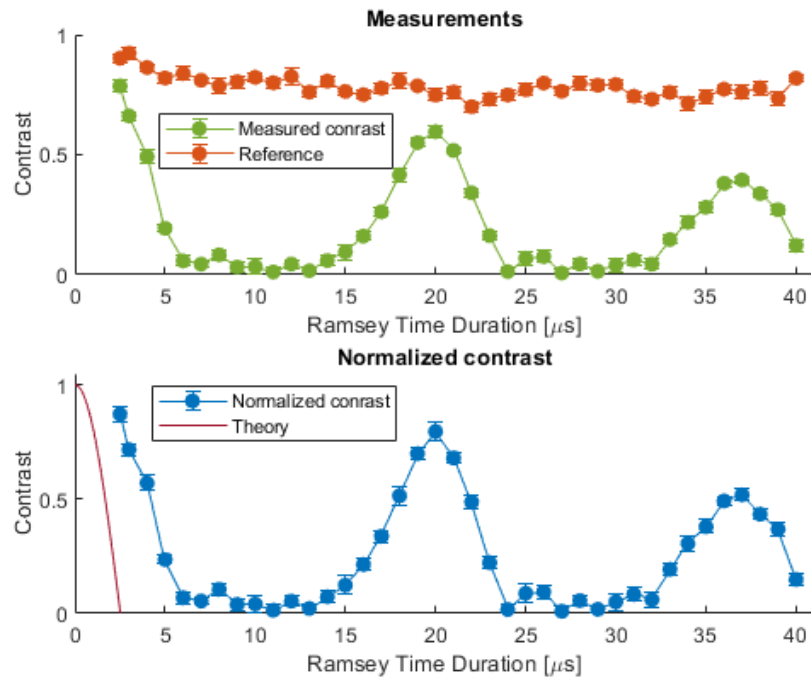


Figure 4.17: Quantum speed limit measurement at 1mW

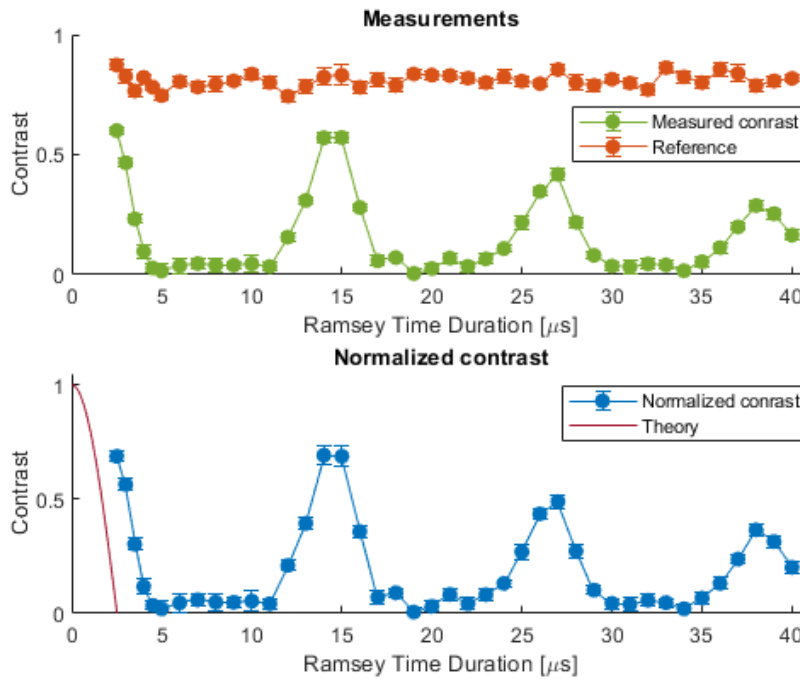


Figure 4.18: Quantum speed limit measurement at 2mW

At the top, each figure shows a direct comparison of the measured contrast in green, with the respective reference points in orange. The lower plot shows the normalized contrast in blue and a comparison with the expected quantum speed limit at that trap depth in red.

Looking at the theoretical prediction from [37], we are looking for the fastest time an atom can change from one orthogonal state to another. Plotting the measured contrasts of the Ramsey fringes for different Ramsey times will show maxima and minima. The time between these two extreme points is the evolution time we are looking for. In the plots, we see the first evolution into the ground state as well as the revivals of the wave function, as expected from figure 4.11. Where the measurement with a trap depth of $14.286\mu\text{K}$ in figure 4.16 shows only one revival, the measurements at higher trap depths exhibit two in case of $28.689\mu\text{K}$ or 3 in case of $57.813\mu\text{K}$. This is explained by the fact that the deeper trap depths correspond to higher trapping frequencies, which allows for more revivals to take place in the same time.

It is also clearly visible that in none of the measurements, the wave function evolves faster from the initial state to the ground state than the theoretical prediction calculated with equation 2.25. The theoretical value for a trap depth of $14\mu\text{K}$ is $\tau_{MT} = 4.357\mu\text{s}$, while the wave function takes around $10\mu\text{s}$ to reach an orthogonal state. Similar measurements for the other trap depths reveal the same result. Our measurements therefore do not break the quantum speed limit, but can be seen as a verification. The discrepancy between the measured evolution time and the calculated speed limit can be explained by several reasons. The atom sample is not completely in the ground state during the entire process and, as we could confirm in chapter 4.3, the atoms are radially hot. Both of these factors could change the actual ΔH , see equation 2.25, as opposed to the theoretical one.

For higher trap depths, the ΔH is larger, which means the minimal evolution time is shorter. This is clearly visible in figure 4.19, where the normalized contrasts of all three trap depths are plotted

together. We immediately see that the yellow trace, which represents the measurement with a trap depth of $57.813\mu\text{K}$, reaches the ground state the fastest, while the blue trace, which represents the measurement with a trap depth of $14.286\mu\text{K}$, is the slowest. The decreasing height of the secondary or tertiary revivals is due to anharmonicities in our optical traps. In an ideal system, where the trapping potentials are perfectly harmonic, we would expect these additional revivals to be of the same height.

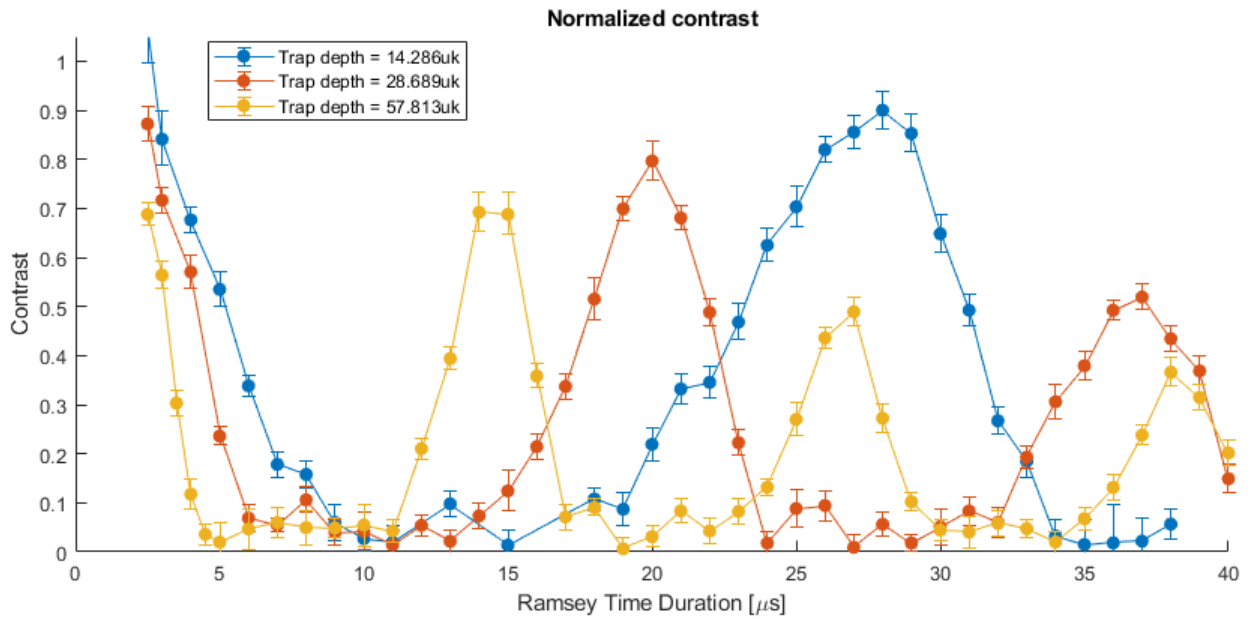


Figure 4.19: Combined plot of the quantum speed limit measurements at different trap depths

Summary and outlook

Summary During my time at the 1D experiment, we modified the Raman laser setup with an AOM, supplementary optics and control circuitry to allow us to produce fast Raman pulses. We have successfully demonstrated our ability to induce Rabi oscillations in a sample of Caesium atoms with Rabi frequencies up to 1.4MHz. We have put this to use to develop a new method to measure the radial temperature in our optical lattice setup and perform Ramsey interferometry.

The temperature measurement made use of the Gaussian intensity distribution of the Raman laser beams addressing the atoms and of the subsequent differences in induced Rabi frequency over the trapped atoms. We were able to model the behaviour and extract the radial temperature at laser powers of up to 1mW per Raman beam.

We performed Ramsey interferometry with the new system, using a Keysight FPGA for the phase modulation of the $\pi/2$ pulses. The new hardware was integrated into the existing experimental sequences and it provides the opportunity to further simplify the setup since three of its output channels are still unused.

The Mandelstam-Tamm speed limit was probed by measuring the evolution of the wave function from its initial to an orthogonal state. This measurement was done by performing Ramsey interferometry with an additional lattice shift between the two characteristic $\pi/2$ pulses. We verified the validity of the quantum speed limit through our measurements, which showed for trap depths of $14.286\mu\text{K}$, $28.689\mu\text{K}$ and $57.813\mu\text{K}$ that the evolution time was slower than the limit predicted through calculation.

Outlook The thermometric measurements were mostly limited by our available laser power. Additional optics to amplify the power of the beams would enable us to closer examine the capabilities of this measurement technique.

In future experimental steps, we plan to change the operating wave length of our optical lattice to 869nm. That way, we make further use of our changed qubit states, since for the new transition, this represents another magical wavelength, this time without any crosstalk in the potentials affecting the two qubit states. This results in a better control of the lattice shift while simultaneously ensuring a stable reference lattice.

The newly integrated FPGA can be used in controlling the lattice beams as a replacement for the currently used DDS's. The advantage would be to use the FPGA to its full capacity and simplify the setup to the extent that these two systems could now be controlled through the same device.

Another possible way to improve our setup would be to use rapid adiabatic passage in state preparation. RAP refers to a method of affecting a change in an atom's state by sweeping the detuning between the driving field and the transition frequency of the desired transition.

With the new qubit transition and the ability to do fast Raman pulses, we can also revisit quantum walk experiments. At the new wavelength, there is no crosstalk to consider, which makes our experiments more precise. Since the Raman pulses are faster than the microwave pulses used in earlier experiments, we will be able to execute more steps in the available coherence time. Here, we can also profit from earlier work on the experiment by Thorsten Groh and Natalie Peter, who developed optimal control ramps which will also improve the speed of the transport and coin operations.

Acknowledgements

At this point I would like to thank all the people who, in one way or another, contributed to this work or supported me in my studies.

Professor Meschede, for the opportunity to work on my Master's thesis in his group and on such an interesting topic.

Dr. Andrea Alberti, who supervised my project and was always able to help when things went wrong. The 1D team, Andreas, Manolo and Gal, for a wonderful lab atmosphere that made working there both challenging and fun.

The rest of the group, for all the help when I needed it, fruitful and relaxing lunch time discussions and the generally great environment, which made this a truly memorable time.

My girlfriend Larissa, who put up with me, even when I felt most stressed, and who always found a way to distract me and cheer me up.

Lastly, my family, for their patient and unwavering support.

Bibliography

- [1] A. M. Kaufman et al. “Two-particle quantum interference in tunnel-coupled optical tweezers”. In: *Science* 345.6194 (2014), pp. 306–309. ISSN: 0036-8075.
DOI: [10.1126/science.1250057](https://doi.org/10.1126/science.1250057).
eprint: <https://science.sciencemag.org/content/345/6194/306.full.pdf>.
URL: <https://science.sciencemag.org/content/345/6194/306> (cit. on p. 1).
- [2] M. Endres et al. *Cold Matter Assembled Atom-by-Atom*. 2016.
arXiv: [1607.03044](https://arxiv.org/abs/1607.03044) [[quant-ph](#)] (cit. on p. 1).
- [3] H. Häffner, C. Roos and R. Blatt. “Quantum computing with trapped ions”. In: *Physics Reports* 469.4 (2008), pp. 155–203. ISSN: 0370-1573.
DOI: <https://doi.org/10.1016/j.physrep.2008.09.003>.
URL: <http://www.sciencedirect.com/science/article/pii/S0370157308003463> (cit. on p. 1).
- [4] A. D. Ludlow et al. “Optical atomic clocks”. In: *Rev. Mod. Phys.* 87 (2 June 2015), pp. 637–701. DOI: [10.1103/RevModPhys.87.637](https://doi.org/10.1103/RevModPhys.87.637).
URL: <https://link.aps.org/doi/10.1103/RevModPhys.87.637> (cit. on p. 1).
- [5] M. Ben Dahan et al. “Bloch Oscillations of Atoms in an Optical Potential”. In: *Phys. Rev. Lett.* 76 (24 June 1996), pp. 4508–4511.
DOI: [10.1103/PhysRevLett.76.4508](https://doi.org/10.1103/PhysRevLett.76.4508).
URL: <https://link.aps.org/doi/10.1103/PhysRevLett.76.4508> (cit. on p. 1).
- [6] T. Groh et al. “Robustness of topologically protected edge states in quantum walk experiments with neutral atoms”. In: *Phys. Rev. A* 94 (1 July 2016), p. 013620.
DOI: [10.1103/PhysRevA.94.013620](https://doi.org/10.1103/PhysRevA.94.013620).
URL: <https://link.aps.org/doi/10.1103/PhysRevA.94.013620> (cit. on p. 1).
- [7] L. Mandelstam and I. Tamm.
“The Uncertainty Relation Between Energy and Time in Non-relativistic Quantum Mechanics”. In: *Selected Papers*. Ed. by B. M. Bolotovskii, V. Y. Frenkel and R. Peierls. Berlin, Heidelberg: Springer Berlin Heidelberg, 1991, pp. 115–123. ISBN: 978-3-642-74626-0.
DOI: [10.1007/978-3-642-74626-0_8](https://doi.org/10.1007/978-3-642-74626-0_8).
URL: https://doi.org/10.1007/978-3-642-74626-0_8 (cit. on p. 1).
- [8] M. R. Grimm and Y. B. Ovchinnikov. *Advances In Atomic, Molecular, and Optical Physics*. 2000 (cit. on p. 3).

- [9] A. Alberti et al. “Decoherence models for discrete-time quantum walks and their application to neutral atom experiments”. In: *New Journal of Physics* 16.12 (Dec. 2014), p. 123052. DOI: [10.1088/1367-2630/16/12/123052](https://doi.org/10.1088/1367-2630/16/12/123052). URL: <https://doi.org/10.1088%2F1367-2630%2F16%2F12%2F123052> (cit. on pp. 5, 44).
- [10] C. G. Townsend et al. “Phase-space density in the magneto-optical trap”. In: *Phys. Rev. A* 52 (2 Aug. 1995), pp. 1423–1440. DOI: [10.1103/PhysRevA.52.1423](https://link.aps.org/doi/10.1103/PhysRevA.52.1423). URL: <https://link.aps.org/doi/10.1103/PhysRevA.52.1423> (cit. on p. 6).
- [11] A. M. Steane, M. Chowdhury and C. J. Foot. “Radiation force in the magneto-optical trap”. In: *J. Opt. Soc. Am. B* 9.12 (Dec. 1992), pp. 2142–2158. DOI: [10.1364/JOSAB.9.002142](http://josab.osa.org/abstract.cfm?URI=josab-9-12-2142). URL: <http://josab.osa.org/abstract.cfm?URI=josab-9-12-2142> (cit. on p. 6).
- [12] *Magneto-optische Falle*. July 2019. URL: https://de.wikipedia.org/wiki/Magneto-optische_Falle (cit. on p. 6).
- [13] J. Dalibard and C. Cohen-Tannoudji. “Laser cooling below the Doppler limit by polarization gradients: simple theoretical models”. In: *J. Opt. Soc. Am. B* 6.11 (Nov. 1989), pp. 2023–2045. DOI: [10.1364/JOSAB.6.002023](http://josab.osa.org/abstract.cfm?URI=josab-6-11-2023). URL: <http://josab.osa.org/abstract.cfm?URI=josab-6-11-2023> (cit. on p. 6).
- [14] C. Robens. “Testing the Quantumness of Atom Trajectories”. In: (2017) (cit. on pp. 6–8, 10–12, 15, 37, 42, 44).
- [15] S. Kuhr. “A controlled quantum system of individual neutral atoms”. In: (2003) (cit. on p. 6).
- [16] W. HAPPER. “Optical Pumping”. In: *Rev. Mod. Phys.* 44 (2 Apr. 1972), pp. 169–249. DOI: [10.1103/RevModPhys.44.169](https://link.aps.org/doi/10.1103/RevModPhys.44.169). URL: <https://link.aps.org/doi/10.1103/RevModPhys.44.169> (cit. on p. 7).
- [17] A. Omont. “Irreducible components of the density matrix. Application to optical pumping”. In: *Progress in Quantum Electronics* 5 (1977), pp. 69–138. ISSN: 0079-6727. DOI: [https://doi.org/10.1016/0079-6727\(79\)90003-X](https://doi.org/10.1016/0079-6727(79)90003-X). URL: <http://www.sciencedirect.com/science/article/pii/007967277990003X> (cit. on p. 7).
- [18] S. Kuhr et al. “Analysis of dephasing mechanisms in a standing-wave dipole trap”. In: *Phys. Rev. A* 72 (2 Aug. 2005), p. 023406. DOI: [10.1103/PhysRevA.72.023406](https://link.aps.org/doi/10.1103/PhysRevA.72.023406). URL: <https://link.aps.org/doi/10.1103/PhysRevA.72.023406> (cit. on pp. 7, 9).
- [19] D. Jaksch et al. “Entanglement of Atoms via Cold Controlled Collisions”. In: *Phys. Rev. Lett.* 82 (9 Mar. 1999), pp. 1975–1978. DOI: [10.1103/PhysRevLett.82.1975](https://link.aps.org/doi/10.1103/PhysRevLett.82.1975). URL: <https://link.aps.org/doi/10.1103/PhysRevLett.82.1975> (cit. on p. 8).
- [20] I. H. Deutsch and P. S. Jessen. “Quantum-state control in optical lattices”. In: *Phys. Rev. A* 57 (3 Mar. 1998), pp. 1972–1986. DOI: [10.1103/PhysRevA.57.1972](https://link.aps.org/doi/10.1103/PhysRevA.57.1972). URL: <https://link.aps.org/doi/10.1103/PhysRevA.57.1972> (cit. on p. 8).

- [21] C. Robens et al.
“Fast, High-Precision Optical Polarization Synthesizer for Ultracold-Atom Experiments”.
In: *Phys. Rev. Applied* 9 (3 Mar. 2018), p. 034016.
DOI: [10.1103/PhysRevApplied.9.034016](https://doi.org/10.1103/PhysRevApplied.9.034016).
URL: <https://link.aps.org/doi/10.1103/PhysRevApplied.9.034016> (cit. on p. 8).
- [22] D. A. Steck. *Cesium D Line Data*. 1998 (cit. on p. 9).
- [23] S. Zienau. “Optical Resonance and Two Level Atoms”.
In: *Physics Bulletin* 26.12 (Dec. 1975), pp. 545–546. DOI: [10.1088/0031-9112/26/12/039](https://doi.org/10.1088/0031-9112/26/12/039).
URL: <https://doi.org/10.1088/0031-9112/26/12/039> (cit. on p. 9).
- [24] N. F. Ramsey. “A Molecular Beam Resonance Method with Separated Oscillating Fields”.
In: *Phys. Rev.* 78 (6 June 1950), pp. 695–699. DOI: [10.1103/PhysRev.78.695](https://doi.org/10.1103/PhysRev.78.695).
URL: <https://link.aps.org/doi/10.1103/PhysRev.78.695> (cit. on p. 10).
- [25] M. F. Andersen, A. Kaplan and N. Davidson.
“Echo Spectroscopy and Quantum Stability of Trapped Atoms”.
In: *Phys. Rev. Lett.* 90 (2 Jan. 2003), p. 023001. DOI: [10.1103/PhysRevLett.90.023001](https://doi.org/10.1103/PhysRevLett.90.023001).
URL: <https://link.aps.org/doi/10.1103/PhysRevLett.90.023001> (cit. on p. 11).
- [26] S. Kuhr et al.
“Coherence Properties and Quantum State Transportation in an Optical Conveyor Belt”.
In: *Phys. Rev. Lett.* 91 (21 Nov. 2003), p. 213002. DOI: [10.1103/PhysRevLett.91.213002](https://doi.org/10.1103/PhysRevLett.91.213002).
URL: <https://link.aps.org/doi/10.1103/PhysRevLett.91.213002> (cit. on p. 11).
- [27] S. Deffner and S. Campbell.
“Quantum speed limits: from Heisenberg’s uncertainty principle to optimal quantum control”.
In: *Journal of Physics A: Mathematical and Theoretical* 50.45 (Oct. 2017), p. 453001.
DOI: [10.1088/1751-8121/aa86c6](https://doi.org/10.1088/1751-8121/aa86c6).
URL: <https://doi.org/10.1088/1751-8121/aa86c6> (cit. on pp. 12, 13).
- [28] L. B. Levitin and T. Toffoli.
“Fundamental Limit on the Rate of Quantum Dynamics: The Unified Bound Is Tight”.
In: *Phys. Rev. Lett.* 103 (16 Oct. 2009), p. 160502.
DOI: [10.1103/PhysRevLett.103.160502](https://doi.org/10.1103/PhysRevLett.103.160502).
URL: <https://link.aps.org/doi/10.1103/PhysRevLett.103.160502> (cit. on p. 13).
- [29] T. Hubert. “Stimulated Raman Transitions Between Hyperfine Ground States of Magnetically Trapped Rubidium-87 Atoms”. MA thesis. Institute of Physics University of Amsterdam, 2015 (cit. on p. 18).
- [30] I. Dotsenko. “Raman spectroscopy of single atoms”. In: (2002) (cit. on p. 20).
- [31] E. A. Donley et al. “Double-pass acousto-optic modulator system”.
In: *Review of Scientific Instruments* 76.6 (2005), p. 063112. DOI: [10.1063/1.1930095](https://doi.org/10.1063/1.1930095).
eprint: <https://doi.org/10.1063/1.1930095>.
URL: <https://doi.org/10.1063/1.1930095> (cit. on p. 22).
- [32] J. J. Snyder. “Paraxial ray analysis of a cat’s-eye retroreflector”.
In: *Appl. Opt.* 14.8 (Aug. 1975), pp. 1825–1828. DOI: [10.1364/AO.14.001825](https://doi.org/10.1364/AO.14.001825).
URL: <http://ao.osa.org/abstract.cfm?URI=ao-14-8-1825> (cit. on p. 22).

- [33] C. Foot. *Atomic physics*. Oxford master series in physics. Oxford University Press, 2005. ISBN: 9780198506966. URL: <https://books.google.de/books?id=kXYpAQAAAJ> (cit. on p. 29).
- [34] Oct. 2019. URL: <http://www.thefouriertransform.com/pairs/box.php> (cit. on p. 38).
- [35] W. Yang, Z.-Y. Wang and R.-B. Liu. “Preserving qubit coherence by dynamical decoupling”. In: *Frontiers of Physics in China* 6.1 (Mar. 2011), pp. 2–14. ISSN: 2095-0470. DOI: [10.1007/s11467-010-0113-8](https://doi.org/10.1007/s11467-010-0113-8). URL: <https://doi.org/10.1007/s11467-010-0113-8> (cit. on p. 42).
- [36] L. Viola and S. Lloyd. “Dynamical suppression of decoherence in two-state quantum systems”. In: *Phys. Rev. A* 58 (4 Oct. 1998), pp. 2733–2744. DOI: [10.1103/PhysRevA.58.2733](https://link.aps.org/doi/10.1103/PhysRevA.58.2733). URL: <https://link.aps.org/doi/10.1103/PhysRevA.58.2733> (cit. on p. 42).
- [37] N. Peter. “Optimal quantum control of atomic wave packets in optical lattices”. In: (2018) (cit. on pp. 46, 47, 53).